CENTRO DE INVESTIGACIONES
EN OPTICA, A.C.

“HYBRID (RAMAN-YTTERBIUM) RING-CAVITY FABRY-PEROT-FILTERED FIBER LASER”

Thesis submitted in fulfillment of the requirements for obtaining the PhD degree in science (Optics) by

Oscar Javier Ballesteros Llanos

Advisor:
Dr. Efraín Mejía Beltrán

León · Guanajuato · México
November 2022

Vo. Bo.
“Versión definitiva.
Incluye cambios sugeridos por revisores”

Dedication

This work is dedicated to God,
to the Llanos family and to
Carolina Rendon Restrepo.

Gratefulness

First of all, I thank God for life and health,
without them it is impossible to achieve
any professional and personal purpose.

To Dr. Efraín Mejía Beltrán, I am infinitely
grateful for the opportunity he gave me
to learn from him as a researcher, teacher,
and above all as a human being. I especially
thank him for his support, the knowledge
transmitted, and the time spent
in my training as a scientist.

Likewise, thanks to the evaluation committee
made up of Dr. Verónica Vázquez,
Dr. Olivier Pottiez and Dr. Yuri Barmenkov
for the follow-up carried out in my
research project.

I thank all the professors, colleagues, and
administrative staff of the CIO, as they
always did an excellent job during
my academic training.

Finally, I thank my entire family for
teaching me to live with ethics, values,
and discipline, thanks to them
I have achieved these academic levels
that today's society demands.

To all, THANK YOU ...

Institutional Acknowledgments

I thank the Consejo Nacional de Ciencia y Tecnología (CONACYT) for the support No.465611 granted through the PhD scholarship (CVU/No.339086 and the project CB-2011-01/166740), which allowed me to finance and consequently obtain the necessary results for the preparation of this work.

As a foreigner, I thank the Centro de Investigaciones en Óptica, A.C (CIO) for the training of human resources and the promotion of scientific and critical thinking in society. At the same time, I thank the CIO for opening their doors to me and allowing me to do my PhD studies in science (Optics), benefiting my academic and professional training.

Abstract

In this thesis, two different main projects were implemented. In the first project, we studied the experimental behavior of nonlinear Raman scattering in a single-mode Nufern 980-HP silica fiber of 1-km in length pumped a 1064-nm. We reconsider some approximations and physical facts that construct the model of Raman amplification. The motivation for this study is based on the fact that the theoretical model neglects the contribution of the small spontaneous Raman scattering (RS) signal; this is what becomes coupled and accumulated along the Raman gain medium (optical fiber), fundamental in the amplification process and; on the other hand, the Raman gain efficiency (g_R) is assumed as a constant parameter for any coupled pump intensity; therefore, the theoretical model does not correspond exactly to the experimental behavior. To consider the small RS signal, we defined a Raman generator coefficient that, added to the differential equations that govern the phenomenon, allowed us to approximate the theoretical model to the experimental behavior, particularly at the threshold where typical models predict a soft Stokes generation; on the contrary, experiments present an abrupt generation. Parallel, we show that the g_R is not a constant parameter.

In the second project, we present the study and the results of the modification of a Raman fiber laser. The study started with the simplest wide spectral emitting free-running distributed feedback configuration, then it was modified to a ring cavity; later, a Fabry-Perot filter was inserted within the feedback loop. Finally, 3-meters of ytterbium-doped fiber was spliced as a Stokes amplifier. In the end, the results show an important performance improvement as the laser configurations evolve; for example, laser emission is stable, less than 1-nm single Stokes line is emitted, the conversion efficiency increased, and the threshold decreased, they compared to the previous configurations. We propose this approach to be used when high stability, high efficiency, and single-line emission is desired in RFLs.

Structure

This thesis is divided into five chapters. Chapter 1 shows a brief introduction to Raman scattering processes involved in Raman fiber laser systems. Chapter 2 proposes

a small modification to the differential equations that model Raman scattering in optical fibers. Chapter 3 shows a small theoretical framework of the electronic and optical properties of rare-earth ions, with a focus on ytterbium (Yb^{+3}) as dopant in vitreous materials. In Chapter 4 the experimental configurations and the methodology implemented to improve the conversion efficiency of RFLs are presented. Finally, in chapter 5 the general conclusions are presented and future works are proposed.

Objectives

In this work, we seek to get closer to understanding the Raman scattering phenomena (spontaneous and stimulated) induced in optical fibers. Understanding the behavior and evolution of the signals (Stokes and residual pumping) involved in the Raman amplification process will allow us in principle to accurately predict the parameters that govern the emission in fiber lasers, this directly impacts the design and the development of these devices. In parallel, we seek to improve emission quality, energy conversion efficiency, and cost reduction in fiber laser systems that can be useful for various scientific and technological applications, since fiber lasers can scale to different wavelengths.

Contents

List of Figures

List of Tables

Introduction

The first optical solid-state laser in the world was demonstrated as a flash-lamp pumped ruby crystal by Theodore H. Maiman in 1960 [2]. Since then, different types of lasers such as gas, liquid, solid-state, free-electron, etc. were demonstrated and developed. Lasers produce and amplify light generating a large flux of output energy; therefore, they are highly directional and very bright. The laser itself is a light source with two very special and important properties, technically called temporal coherence and spatial coherence. The first refers to the invariability of the wavelength, frequency and phase velocity of the beam that propagates space-time; while the second is the ability of the waves emitted by the laser to maintain the constant phase difference between two spatially separated points. The light produced in a laser system is composed of ordered and identical photons that propagate in the same direction. This implies that the individual light waves, emitted by the laser, are all of the same wavelength (main characteristic of monochromatic light) and are all in phase, the reason for the latter being their high brightness. This allows for a concentration of energy in a finely defined area.

Monochromatic radiation sources are characterized in that their intensity remains constant in time I(t) = constant, and the bandwidth of their spectral line in frequency is approximately zero ($\Delta\omega \approx 0$). For its part, in a Q-Switching type laser radiation source (Q switching), the intensity of the beam varies over time, generating long pulses ($\tau \gg$) and its frequency spectrum has a small bandwidth ($\Delta\omega \ll$). Another source of laser radiation is the well-known Mode locking, where the intensity variation in short times ($\tau \ll$) is translated into short pulses; therefore, its frequency spectrum has a wide bandwidth ($\Delta\omega \gg$). Finally, we have the supercontinuous source that generates ultrashort pulses in very short times ($\tau \lll$) and its frequency spectrum is very large ($\Delta\omega \ggg$); furthermore, the ultra-high peak intensities generate more pulses with more frequencies based on non-linear effects; for this reason they are known as supercontinuous sources, their spectrum becomes so broad that it can be considered as white light. Several decades of work have improved laser performance, whereas at the same time it has been playing increasingly important roles in scientific research, defense and information technology, manufacturing, and material processing and many more areas.

Of the variety of lasers available on the market, solid-state lasers (semiconductor lasers, glass and crystal lasers, fiber lasers, and solid-state dye lasers) are the preferred coherent source for various scientific and industrial applications due to their superior performance and robustness. The efficiency of solid-state lasers is generally higher than that of gas lasers (Helium-Neon, Argon), and both continuous wave (CW) and pulsed output can be achieved with an output power range from a few milliwatts to several tens of kilowatts. Among solid-state lasers, fiber laser (FL) exhibits many advantages over its counterparts because their great length of active medium absorbs the pump more efficiently and they present a larger gain length; which allows a total superposition of the beams (pump and laser signal); such attributes, make this type of lasers highly efficient [3]. Their cavities, although lengthy, can be rolled up to make them to be semi-compact. As the cavities are generally formed by mirrors (they may be the facets of the perpendicularly cleaved fiber ends), fiber Bragg gratings attached to the fiber ends, or even thin and small bulk mirrors, these laser devices present a very stable alignment and are immune to vibrations and external electromagnetic fields. In FLs, the spatial distribution of the laser signal is well confined within the center (core) of the fiber structure, guaranteeing excellent beam quality and stability. Low cavity losses lead to high optical conversion efficiencies and its excellent heat dissipation capacity, due to the large surface-to-volume ratio that allow room-temperature operation, ensure the success of fiber lasers that can be small in volume and weight. The main advantage of the FL is that practically any laser wavelength, from ultraviolet to infrared, can be achieved with a suitable choice of the pump wavelength, as long as the wavelengths are within the transparency region of the fiber material. In general, the beams from these lasers are easy to manipulate to be deposited with high precision in the desired place.

A specific type of FL is the Raman fiber laser (RFL) that operates from the stimulated Raman scattering (SRS) produced by the molecular vibrations of the fiber material when excited at high powers [4]. This non-linear behavior transfers pump energy to frequency-shifted Stokes components (to a lesser degree to anti-Stokes components) and as an attribute, amplified signals are obtained that operate and can scale in the spectral region from 1100 to 1700 nm when pumped above 1000 nm. Currently, RFLs are the only wavelength scalable, high power fiber laser technology that can span the wavelength spectrum [5]. One of the most important parameters in the design of RFLs and Raman fiber amplifiers (RFA's) is the Raman gain efficiency (g_R), which mainly depends on the input pump power, fiber length, effective core area, the Raman cross-sections, and the Raman gain coefficient. The g_R has been widely studied with experimental techniques and analytical solutions based on assumptions [6], leading to a mathematical equation that approximately relates the g_R with experimental variables [7]. The formula comes from an analytical solution to

the set of differential equations governing the SRS [8], and the variables that compose it can be measured experimentally with relative ease at specific points such as Raman threshold, critical power, etc. Beyond the threshold, the analytical solution presents uncertainty due to the complexity involved in measuring the small non-linear signal of spontaneous Raman scattering (RS), equivalent to the seed of the amplification process. Understanding the behavior and evolution of the RS signal along an optical fiber (before, during, and after the Raman threshold), will allow us to accurately estimate the g_R. For this reason, in one of our works we reconsidered some approximations and the physical facts that construct the model of Raman amplification; and with experimental data, we quantified the g_R in a single-mode Nufern 980-HP silica fiber of 1-km in length. We show that the g_R is not a constant parameter as it is considered in most of the reported works. To approximate the mathematical model even closer to the experimental behavior, we consider the small RS signal and define a Raman generator coefficient (R_{GC}) that is added to the differential equations that model the evolution of the signals involved (first Stokes and pump residual). With this study, we managed to approximate the theoretical model to the experimental behavior in particular at the threshold.

On the other hand, to achieve single-frequency output and improve conversion efficiency in RFLs, several configurations have been implemented, among which stand out: distributed feedback (DFB) fiber laser, short cavity distributed Bragg reflector (DBR) fiber lasers, ring cavity fiber laser with embedded narrow-bandwidth filters, hybrid configurations with rare-earths ion-doped cavities, etc. We propose a hybrid laser configuration that can be useful when high stability, high efficiency, and single line emission are desired in RFLs. The experimental approach begins from the simplest wide spectral multiband and multiaxial mode emitting free-running distributed feedback configuration, then it was modified to a ring cavity that eliminated one band; later, a Fabry-Perot (FP) filter was inserted within the feedback loop to generate single-line emission. Finally, a small piece of ytterbium-doped fiber was spliced as a Stokes amplifier. The results show an important performance improvement as the aforementioned laser configuration evolves. The optimization of some parameters of this non-optimum system opens up opportunities to take it as a base for high-power hybrid FLs.

All the aforementioned topics are described in detail throughout this thesis work. Several aspects are left open for further investigation.

Chapter 1

Raman Fiber Lasers Physical Fundamentals

1.1 Introduction

The Raman fiber laser (RFL) is a specific type of laser in which the fundamental mechanism, to amplify the light, is stimulated Raman scattering (SRS). This fact contrasts with most conventional lasers (lasers based on bulk crystals as gain media), which rely on stimulated electronic transitions as an amplification mechanism. The RFLs are optically pumped; however, this pump does not produce a population inversion as in conventional lasers; rather, the pump photons are frequency shifted and scattered by the electrical dipole behavior of the molecules (SiO_2, GeO_2, P_2O_5)[1] that form the fiber-cores; in this way, the new frequencies oscillate in a coherent way (constant phase ratio), time-delayed and shifted with respect to the pump frequency. Therefore, if the frequency-shifted is greater than the pump-frequency, the scattering signal is an anti-stokes; but if the frequency-shifted is lower, a Stokes signal takes place. For its part, the difference between the energy of the pump photons and the energy of the photons-shifted is within a band that corresponds to vibrational frequencies of the gain media [9]; e.g., the Raman shift in phosphor-silicate fibers is ∼39.9 THz (∼1330 cm^{-1}), whereas this shift on germanium-silicate glass is ∼13.2 THz (∼440 cm^{-1}) [10, 11]. This allows us, in principle, to produce arbitrary wavelengths if we choose the pump wavelength appropriately [12]. This behavior differs from conventional lasers, in which the possible output wavelengths are determined by the emission lines of the gain medium.

The first continuous-wave Raman laser in fiber was demonstrated in 1976 [13]. Pumping at the watts level, a distributed Raman gain, higher than the linear attenuation plus losses at splice points, was induced in a single-mode glass fiber, placed inside a Fabry-Perot cavity. Although RFLs have been widely investigated since then,

[1] Silicon Oxide, Germanium Oxide, Phosphorous Oxide

the development of new materials and new technology in fiber optic manufacturing have marked the path to the research and implementation of new setups, with the aim of reducing the operating threshold, improve efficiency, and power stability. Next, let us describe the physical foundations under which Raman fiber lasers operate.

1.2 Raman Scattering in optical fibers

The first theories about the scattering of light were given by Smekal in 1923 [14]. He predicted sidebands in the spectrum scattered light by considering a two-level quantum model. In 1925 Raman observed for the first time that scattered light, in a benzene-based liquid, exhibited a frequency shift, and by 1928 he noticed that this scattering was polarized [15]. Later, in 1962 Woodbury and Ng observed, accidentally and experimentally, the appearance of lines with higher frequency than usual in a ruby laser. However, it was Eckhardt, et al. who recognized this phenomenon as stimulated Raman scattering [16].

Scattering phenomena are classified by the relation between the frequencies of the incident photon and the scattered photon. If the frequencies of both photons are equal, it is said that there is conservation of energy, it is elastic Rayleigh scattering [17]. But if these frequencies differ (photon scattered with less or greater frequency); then, there is no longer energy conservation, so the process is inelastic; e.g., Raman scattering. The latter process can be described as the interaction of a photon with an optical phonon [18], which originates from a finite response time of the non-linear third-order polarization of the material [19] and, additionally, it can reveal information about the structure and dynamics of materials when light is scattered by abnormalities present in the medium. Two types of Raman scattering are of interest for their consequences in diverse fields: Spontaneous Raman Scattering (RS) and Stimulated Raman Scattering (SRS). Let us describe them right away.

1.2.1 Spontaneous Raman Scattering (RS)

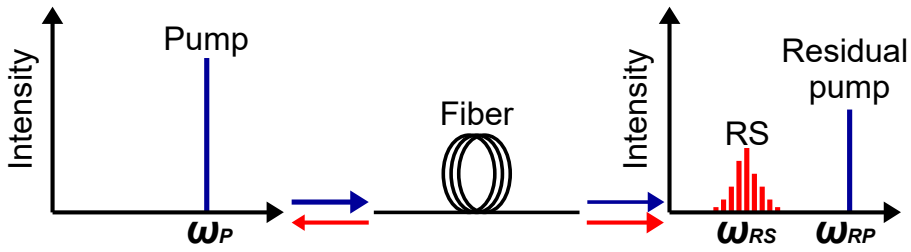

Figure 1.1: Spontaneous Raman scattering phenomenon.

When a monochromatic light beam propagates (ω_P) in an optical fiber, spontaneous Raman scattering occurs. This process transfers some of the photons to new frequen-

cies (ω_{RS}), see Figure 1.1. The light beam exhibits some absorption losses when it propagates through a homogeneous and isotropic medium. However, if the material is not completely homogeneous, especially if the inhomogeneities are comparable in size to the wavelength of the light, it will scatter with an anisotropic distribution; i.e., with a privileged direction over the entire solid angle (4π) [17]. If the material shows only fixed spatial inhomogeneities, there will be no change in frequency of the scattered light; i.e., light will scatter elastically (Rayleigh scattering). Nevertheless, due to temperature variations, slight modulations of the refractive index occur through the molecular vibration of the material; therefore, inelastic components are added [18]. In this case, part of the scattered light will show emission lines wavelength-shifted due to these vibrations (Raman scattering) [20].

Raman scattering is an inelastic light-matter interaction and it is a weak effect in comparison to Rayleigh scattering, let's see. A photon with energy $E = \hbar\omega_p = \hbar 2\pi f_p$ ($\hbar = h/2\pi$; h = Planck's constant; ω_p = angular frequency; f_p = frequency) traveling through a material can transfer energy and momentum $\vec{P} = \hbar\vec{k}$ ($\vec{k}$=wave vector) to the natural vibrations of the molecules present in the medium; therefore, the structure will have a perturbation due to the dipole moment. From a quantum perspective, the annihilation of an incident photon and creating a scattered photon corresponds to the Raman effect [21]. Next, we review the functions that describe the state of the system in terms of the position and moment variables [22]. The total Hamiltonian of the system can be described as follows:

$$H_{tot} = H_{vib} + H_{EB} + H_{int} \tag{1.1}$$

where H_{vib}, H_{EB}, and H_{int} are the vibrational, electromagnetic, and interaction Hamiltonian, respectively. Let us quickly describe them below.

$$H_{vib} = \frac{\vec{P}^2 + (\Omega m\vec{q})^2}{2m} \tag{1.2}$$

Equation (1.2) contains the kinetic and potential energy of the system. ($\vec{P}$) is the momentum, (Ω) is the vibrational frequency of the fundamental mode of the system, (m) is the mass of the molecule, and ($\vec{q}$) is the local coordinates vector.

Term H_{EB} (from equation 1.1) is the Hamiltonian that depends on the electric $\vec{E}$ and the magnetic $\vec{B}$ fields, and quantizes the radiation field present in the system as described in [18]:

$$H_{EB} = \frac{\vec{E}^2 + \vec{B}^2}{2} \tag{1.3}$$

For its part, H_{int} can be obtained from the electric displacement field ($\vec{D}$), which depends on the electric permittivity (ε) (equation 1.4). Where ε_0 is the vacuum permittivity, $\vec{\chi}$ is the electric susceptibility, and $\vec{P}$ is the polarization density.

$$\vec{D} = \varepsilon \cdot \vec{E} = \varepsilon_0(1 + \vec{\chi}) \cdot \vec{E} = \varepsilon_0\vec{E} + \varepsilon_0\vec{\chi}\vec{E} = \varepsilon_0\vec{E} + \vec{P} \tag{1.4}$$

Now, during the interaction of the material with the incident wave, the electric field of said wave induces an electric dipole moment ($\vec{p}$)[19]. If the material is now considered to have anisotropy, then the electrical permittivity depends on the location within the medium and the angular frequency of the incident wave; therefore, it has a time-dependent response. From this premise, the polarization as a function of time is defined as follows:

$$\vec{P}(t) = \varepsilon_0\vec{\chi}(t)\vec{E}(t) = N\vec{p}(t) = N\vec{\alpha}(t)\vec{E}(t) \tag{1.5}$$

where N is the number of molecules per volume unit present in the system, $\vec{p}$(t) is the electric dipole moment as a function of time, and $\vec{\alpha}$(t) is the molecular optical polarizability tensor. Then the interaction Hamiltonian (H_{int}) between the dipole moment and the external electric field results in the following equation:

$$H_{int} = \vec{E}(t) \cdot \vec{P}(t) = \vec{E}(t) \cdot N\vec{\alpha}(t)\vec{E}(t) \tag{1.6}$$

where $\vec{\alpha}(t)$ is the molecular polarizability, which can be expressed as a function of general coordinates vector $\vec{q}$(t) as follows:

$$\vec{\alpha}(t) = \alpha_0 + \left(\frac{\partial\vec{\alpha}}{\partial\vec{q}}\right)_{q_0} d\vec{q}(t) \tag{1.7}$$

Here $d\vec{q}(t)$ is the displacement from the equilibrium molecular length q_o such that:

$$d\vec{q}(t) = dq_o e^{(\pm it\Omega)} \tag{1.8}$$

Then, the interaction Hamiltonian can be expressed as:

$$H_{int} = \vec{E}(t) \cdot \vec{P}(t) = \underbrace{\vec{E}(t) \cdot N\alpha_0\vec{E}(t)}_{A} + \underbrace{\vec{E}(t) \cdot \left(\frac{\partial\vec{\alpha}}{\partial\vec{q}}\right)_{q_0} d\vec{q}(t)\vec{E}(t)}_{B} \tag{1.9}$$

In equation (1.9), the term “A” corresponds to the linear optical phenomenon (elastic scattering); e.g., Rayleigh scattering, and the term “B” is nonlinear because the output

frequency is different from input one (inelastic scattering); e.g., spontaneous Raman scattering. The latter can be seen more clearly by considering $\vec{E}(\omega,t) = E_0 e^{i\omega_p t}$ and $\vec{q}(t) = q_0 e^{\pm i\Omega t}$, where ω_p is the frequency of the incident beam and Ω is the frequency of molecular oscillation. $\vec{p}(t)$ can be obtained as [11]:

$$\vec{p}(t) = \alpha_0 E_0 e^{i\omega_p t} + \left(\frac{\partial\vec{\alpha}}{\partial\vec{q}}\right)_{q_0} dq_0 E_0 e^{it(\omega_p \pm \Omega)} \tag{1.10}$$

Therefore, the polarization vector $\vec{P}(t)$ is defined as dipole moment per unit volume. If there are N dipoles per unit volume, then:

$$\vec{P}(t) = N \cdot \vec{p}(t) = N\left[\alpha_0 E_0 e^{i\omega_p t} + \left(\frac{\partial\vec{\alpha}}{\partial\vec{q}}\right)_{q_0} dq_0 E_0 e^{it(\omega_p \pm \Omega)}\right] \tag{1.11}$$

Assuming the interaction of a molecular system with a harmonic electric field, a pumping source of angular frequency ω_p, one can interpret the Raman scattering as the interaction between pump photons with energy $\hbar\omega_p$ and arrangement of molecules with a system of states E_1 (ground state) and E_2 (vibration state) as in Figure 1.2.

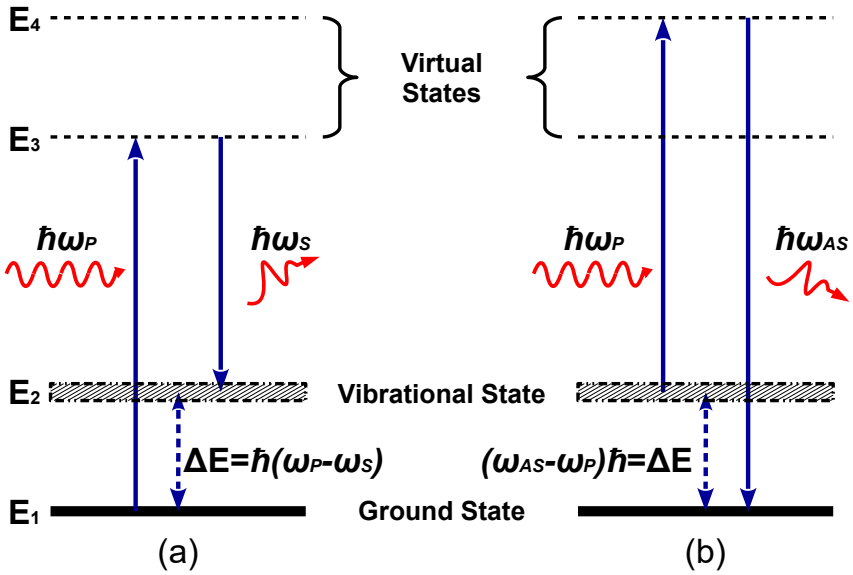

Figure 1.2: Energy diagram for Raman Scattering process. a) Stokes shift; b) anti-Stokes shift.

Let's assume that the molecule in thermal equilibrium is vibrating in the ground state E_1. By interacting with the photon, it could be excited to the virtual state E_3 (molecular polarizability) with energy $E_1 + \hbar\omega_p$. Once the molecule instantaneously takes the energy of the photon through the polarizability, a resonant phonon with energy $E_1 - E_0$ "steals" energy from the photon to elevate molecular vibration to E_2. Then, the photon becomes energy-reduced to be scattering with energy $E_3 - E_2$ as in Fig.1.2a. It suffers in this way a Stokes shift. Here, the final state E_2 is of higher

energy than the initial state E_1 and the energy difference $\triangle E = \hbar(\omega_p - \omega_S)$ converts into the vibration of the molecule, i.e., a phonon is excited. Therefore, the angular frequency ω_S of the emitted Stokes photon is lower than the frequency of the incident photon, and its energy is $\hbar\omega_S = \hbar\omega_p - \Delta E$. For its part, if it returns to the ground state E_1, then it is an elastic scattering (Rayleigh scattering). Fig. 1.2b shows the Raman anti-Stokes scattering. Here, the initial state is E_2, the intermediate state E_4, the final state is E_1 and $\triangle E = \hbar(\omega_{AS} - \omega_p)$ is the energy difference. By interacting with an incident photon, the molecule is excited to the virtual state E_4 with energy $E_2 + \hbar\omega_p$ and may drop spontaneously to the lowest energy level E_1. When this happens, the angular frequency ω_{AS} and the energy $\hbar\omega_{AS} = \hbar\omega_p + \Delta E$ of the emitted anti-Stokes photon will be greater than the incident photon. In such a case, the phonons provide energy to the photons.

Both Stokes and anti-Stokes scattering are temperature-dependent [23], and they are governed by the Boltzmann distribution as $e^{\pm\hbar\omega_s/k_B T}$, where k_B is the Boltzmann constant and T is the absolute temperature. In a state of thermal equilibrium, the population of the ground state E_1 is higher compared to the vibrational state E_2 so the anti-Stokes scattering is weaker than the Stokes scattering process. Therefore, the spontaneous Raman scattering is dominated by the Stokes shifts [24]. Furthermore, at low temperatures, the strength of Stokes scattering rises to a constant value and the strength of anti-Stokes scattering decays to zero; whereas, at high temperatures, the anti-Stokes scattering strength approaches Stokes scattering strength [19].

1.2.2 Stimulated Raman Scattering (SRS)

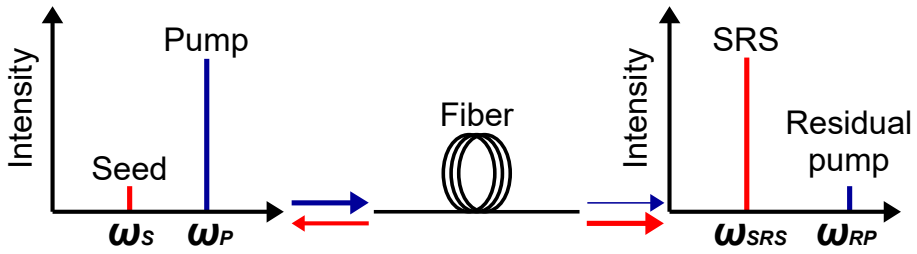

Figure 1.3: Stimulated Raman scattering phenomenon.

In a medium, such as an optical fiber, spontaneous Raman scattering (RS) occurs when a coupled signal (pump) has low power levels. In this case, the core molecules contribute to the RS process by vibrating independently and, therefore, there is no directionality of the scattered light. The fraction of Raman-scattered light (typically 10^{-6}cm^{-1} of the pump power); coincides with the numerical aperture (NA) of the fiber and is guided along its axis, in both directions (forward and backward, see Fig.1.3), being attenuated by the background losses of the fiber. But, by increasing the power of the pump signal to levels where the molecules are not able to harmonically follow the

sinusoidal behavior of the electric field (supposing it is monochromatic), what happens now is that the polarizability of the molecules generates new oscillating frequencies, spectral broadening in this way the propagating pump signal. Hence, some spectral components coincide with the Stokes signal and make the molecules to behave as an array of vibrating oscillators that generate phase-aligned photons; i.e., they oscillate coherently. In this case, the Stokes photons of the small RS signal (see Fig.1.4a), which coincide with the phase-aligned photons, cause an avalanche process where pump photons are annihilated and the Stokes photons are amplified (this is energy transfer, see Fig.1.4b), generating a gain that exceeds the intrinsic losses of the fiber, once the pump power exceeds a threshold value. Under this behavior, the molecules migrate to a high-vibrating mode [25]; in other words, this phenomenon should be considered as a one-step process, in which three events occur almost simultaneously: absorption of the incident photon, emission and amplification of the Raman scattered photon, and transition of the molecule to an excited state. On the other hand, the process of absorption of a Stokes photon, represented by the green arrow, is very unlikely to occur because of the immediacy with which the phonon-assisted transition operates after the molecule emits a Stokes photon.

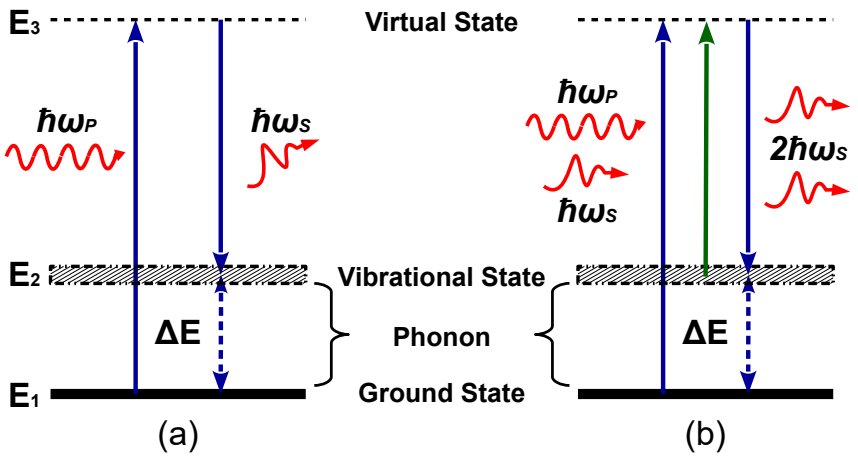

Figure 1.4: Raman scattering processes. a) RS, and b) SRS.

This is the stimulated version of RS known as stimulated Raman scattering (SRS), which usually emits a spectral linewidth narrower than the spontaneous linewidth [26] and its energy is determined by the material as $E_1 + \hbar\omega_p = \Delta E + \hbar\omega_S = E_2 + \hbar\omega_S$ [19]. The SRS has been used as a platform for the development of Raman fiber lasers and amplifiers [27].

1.2.3 Raman gain spectrum

The Raman gain spectrum represents the intensity of the Stokes waves as a function of the frequency shift ($\Delta\omega = \omega_{pump} - \omega_{stokes}$). Raman shift that arises from modulations to the molecular polarizability by the vibrational states of the molecules present in the

fiber [28]. This behavior depends on the decay time related to the excited vibrational state. As a result, the Stokes waves depend on the pump frequency [1]. The Raman gain spectrum can be determined by direct measurement of the gain experienced by a Stokes wave through SRS after propagating through an optical fiber. For pure silica fibers, the Raman gain spectrum (Fig.1.5) extends up to ∼1333 cm^{-1} (∼40 THz) with a bandwidth (ΔV_R) of ∼466.6 cm^{-1} (∼14 THz) and two dominant peaks at 440 cm^{-1} (13.2 THz) and 500 cm^{-1} (15 THz), whose magnitudes are inversely proportional to the effective area of the core [28]. It is often useful to consider the conversion between cm^{-1} and THz, which is done through the following relationship: $f(\text{Hz}) = c \cdot f(cm^{-1})$, where c is the speed of light (299.792.458 m/s ≈ 3x10^8 m/s).

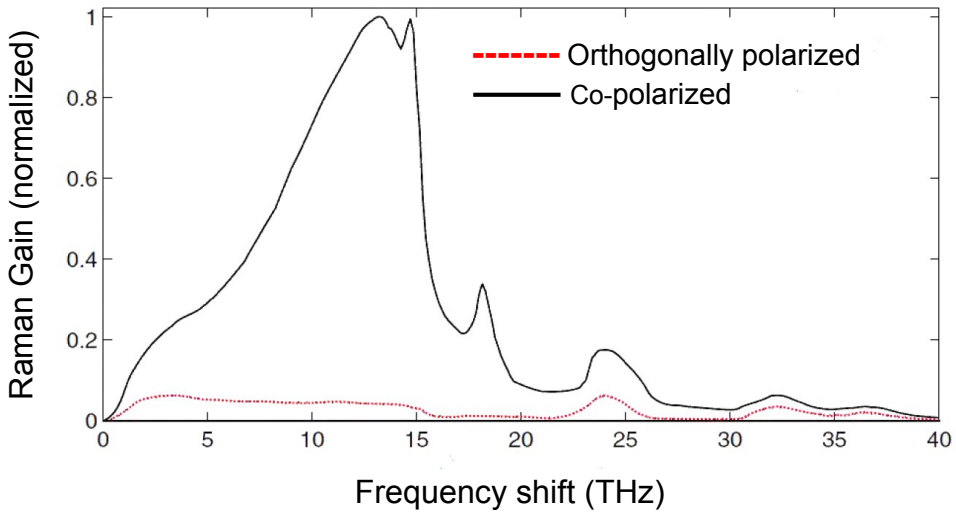

Figure 1.5: Spectrum of Raman gain for fused silica at pump wavelength ∼1000 nm. When signals (pump and Stokes), are co-polarized and orthogonally polarized. Spectra are normalized to the peak of the co-polarized spectrum [1].

The amorphous nature of silica is responsible for the large bandwidth and the multiple peaks in the Raman gain spectrum [19]. Note that this spectrum is polarization-dependent. Fig.1.5 shows two normalized Raman gain spectra for silica, measured when the pump and signal light were either co-polarized or orthogonally polarized. The peak gain, when they are co-polarized, is approximately an order of magnitude larger than when they are orthogonal. This applies not only for linearly polarized light, but also in general for elliptical states of polarization [29]. For example, in typical long fibers, which do not maintain linear polarization, the Raman gain will assume some average value which is approximately half of the polarized gain [30].

The Raman gain is associated with a Raman gain term (g_r) that is related to optical gain ($g(z)$) [1, 31] as:

$$g(z) = g_r I_p(z) = \frac{g_r}{A_{eff}} P_p(z) = g_R P_p(z) \tag{1.12}$$

Where I_p and P_p are the intensity and power of the pump respectively, and $A_{eff} = \pi W_o^2$ [m^2] is the effective core area of the fiber (W_o corresponds to the mode field area; which interacts with the pump beam along an optical fiber). For its part, g_R is the Raman gain efficiency and is defined as $g_R = g_r/A_{eff}$ $[m^{-1}W^{-1}]$, where g_r was normalized to $1 \times 10^{-13} \frac{m}{W}$ for a pump wavelength $\lambda_P = 1000nm$; but for other pump wavelengths, g_r is obtained from the following relationship [32, 33]:

$$g_r(\lambda_p) = \left(\frac{1000nm}{\lambda_p}\right)\left(1 \times 10^{-13}\frac{m}{W}\right) \tag{1.13}$$

Note that g_r is inversely proportional to the wavelength of the pump. So if the pump is 1064 nm, then g_r is $\approx 9.4 \times 10^{-14}$ m/W and the peak value of the gain term becomes centered at 1116 nm, this implies that 13.2 THz corresponds approximately to 52 nm.

1.2.4 Propagation equations for Raman scattering along an optical fiber

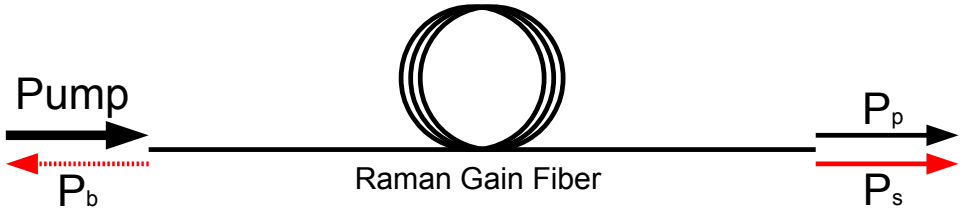

Figure 1.6: Forward and backward propagation in silica fiber

When a high-power pump signal is coupled at the core of an optical fiber, stimulated Raman scattering (SRS) is generated and these scattered signals (Stokes and anti-Stokes) propagates along the fiber at both directions (forward and backward). The differential equations that describe the propagation of pump power (P_p), the forward Stokes power (P_s), and the backward Stokes power (P_b) are defined as follows [34]:

$$\frac{dP_p}{dz} = -\alpha_p P_p - \frac{\nu_p}{\nu_s}\frac{g_r}{A_{eff}}P_p(P_s + P_b) \tag{1.14}$$

$$\frac{dP_s}{dz} = -\alpha_s P_s + \frac{g_r}{A_{eff}}P_p P_s \tag{1.15}$$

$$\frac{dP_b}{dz} = \alpha_s P_b - \frac{g_r}{A_{eff}}P_p P_b \tag{1.16}$$

The first term on the right side of each equation is due to the linear absorption in the fiber medium, where α_p and α_s are the pump and Stokes values of the intrinsic loss [Km^{-1}] of the host glass (i.e., attenuation/absorption coefficients) at each particular

frequency (ν_p and ν_s). The second terms on the right sides of the equations describe the nonlinear stimulated process and couple the three waves together. A_{eff} is the effective core area of the single-mode fiber, g_r is the Raman gain term defined in the previous section and, z is the distance [Km] measured along the fiber. Graphically, Figure 1.7 shows the pump-dependent output energies for residual pump and first Stokes.

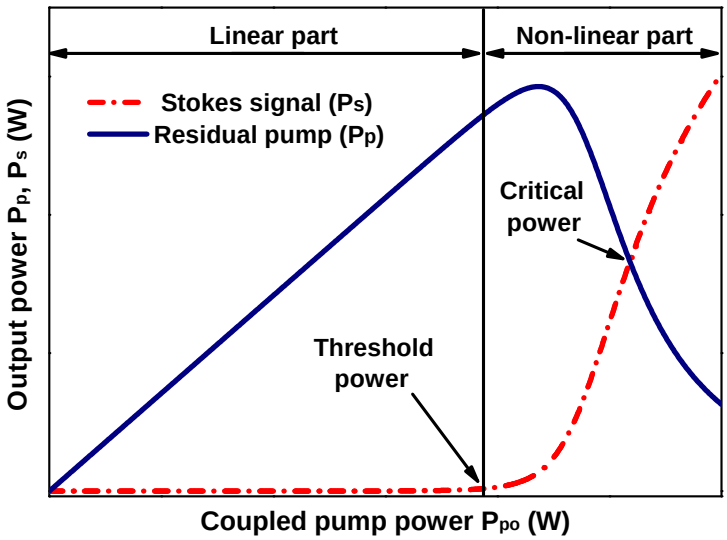

Figure 1.7: Transfer of pump energy to the first Stokes as a function of the coupled power.

In general, the Raman gain efficiency (g_R) depends on various parameters, such as absorption coefficient, atomic mass, refractive index, optical frequency and molecular density [35]. The g_R can be estimated quite accurately by the analytical solution of the differential equations that govern the SRS and that are related to experimental variables [36]. In Chapter 2, we will discuss the propagation equations to quantify threshold power, critical power, and Raman gain efficiency, in an HP-980 fiber, as they are important parameters in the design of Raman fiber lasers and amplifiers.

1.3 Raman Fiber Amplifier (RFA)

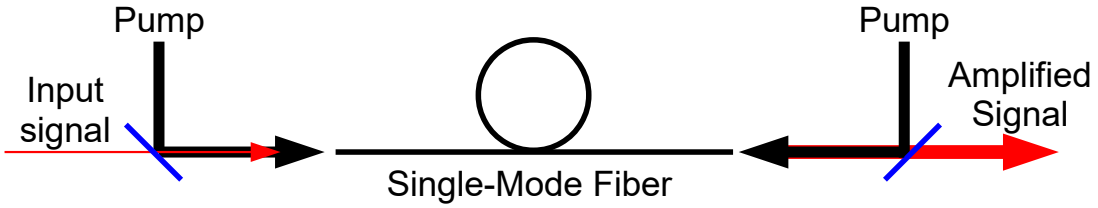

Figure 1.8: Schematic of Raman fiber amplifier showing the signal and pump directions.

The foundation of an optical amplifier is the stimulated emission process just like in a laser. Their structure is similar, but they differ in that it does not have feedback to make the device oscillate, so it can only raise the power level of an incident signal. Optical amplification has had a great impact on applications that use fiber optics [37]. Nowadays, these amplifiers are not only useful in optical communications, but are also used in systems where it is necessary to increase the power of certain weak signals with unique characteristics of coherence, momo-chromaticity, pulsed, etc. The RFA's are devices that do not require special dopants; therefore, passive, transparent, and ordinary optical fibers can be turned into a Raman amplifier; this is very useful because Raman gain can be achieved in any conventional transmission fiber, allowing Raman amplification to be compatible with most available transmission systems [38]. For its part, Raman amplification can be provided at any wavelength. Being the Raman gain non-resonant, it is available over the entire transparency region of fiber ranging from approximately 0.3 μm to 2 μm [39], if the appropriate pump sources are available. Very important, Raman gain has a high-speed response [40]; therefore, in principle, the entire bitstream can be amplified without any distortion in high-bit-rate systems (in fiber).

1.4 Raman Fiber Lasers (RFLs)

A Raman fiber laser (RFL) is a fiber resonator at the Stokes wavelength, in which SRS shifts the spectrum of the propagating pump radiation through an optical fiber towards (usually) lower frequency Stokes components. The basic scheme of an RFL, in general, requires three key elements: a low effective-area and high-nonlinearity optical fiber for providing Raman gain, mirrors for feedback, and components for isolation between the pump laser (usually a rare-earth-doped fiber laser) and the Raman resonator.

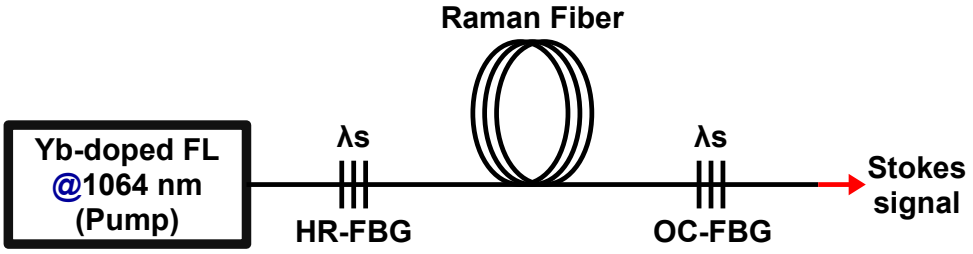

Figure 1.9: Schematic representation of a Raman fiber laser with one wavelength shift (HR -highreflectivity fiber Bragg grating, OC - output coupler a low-reflectivity fiber Bragg grating)

In RFLs, lasing occurs when the Raman-active gain medium (which is pumped) is placed inside a cavity, for example, between mirrors reflecting and trap part the Stokes wavelength λ_s (see Fig.1.9). By increasing the pump power, the system reaches

a threshold power that is obtained when Raman amplification, during a round trip, is as large as to compensate for the cavity losses. In an all-fiber configuration, enough positive feedback for lasing at the first Stokes wavelength is easily achieved and directionality of the laser emission is provided, in most cases, by a high-reflectivity fiber Bragg grating (HR-FBG $> 99\%$) on the input side and by a low-reflectivity output coupler (OC-FBG at Stokes wavelength) on the output side. In addition, it is worth highlighting the unique property of Raman laser, i.e., they can be operated at several wavelengths simultaneously. Higher-order Stokes wavelengths can be generated inside the active medium at high pump powers, and they simultaneously oscillate in association with their separate sets of mirrors for each Stokes beam [41] as seen in Figure 1.10.

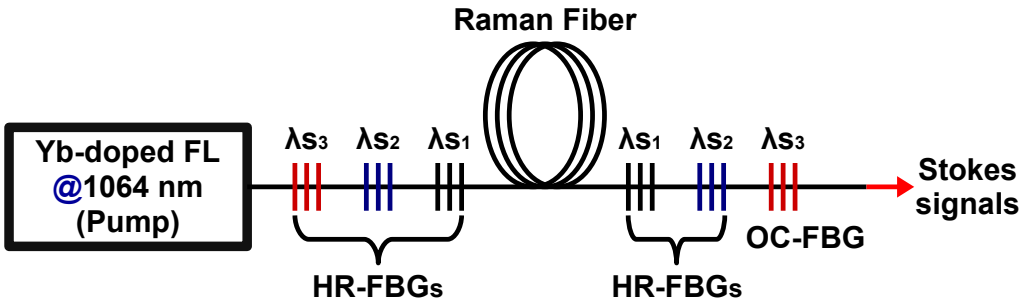

Figure 1.10: Schematic representation of a Raman fiber laser with multiple wavelengths emission in a cascaded Raman resonator configuration (HR - high-reflectivity fiber Bragg grating, OC - output coupler with low-reflectivity fiber Bragg grating)

It is worth highlighting that there are some important differences between RFLs and traditional lasers. One of them is that in an amplifier based on Raman gain, no stimulated emission from excited atoms or ions takes place. A second one is that the required wavelength for pump the Raman laser does not depend on the electronic structure of the medium, so the pump can be chosen to minimize absorption.

Chapter 2

Modifications proposal to the modeling of the Stokes signal in Raman fiber lasers.

2.1 Abstract

In this thesis, we propose some changes to the theoretical model that simulates the Raman scattering, both linear and nonlinear, in single-mode optical fibers. The changes introduced in the mathematical model were supported by approximations based on physical phenomenology, as well as on direct measurements realized during characterizations 1-km fiber (Nufern 980-HP) laser. In particular, our interest was based on the abrupt (experimental) generation of stokes signal when reaching the nonlinear stimulating Raman scattering; in our proposal, we consider the optical fiber as capturing and accumulating the close to axis small, Raman, signal produced by the pump as it propagates along the fiber. Instead of the soft growth of the Raman signal as the intensity of the pump increases, as reported to date, our model describes the step of the emitted Stokes signal when the threshold is reached. The fact that at this point, the isotropically generated Raman signal is inhibited in-axis does not prevent the amplification caused by the stimulated Raman scattering from redirecting these photons so that they propagate coherently along the optical fibers. In this way, depending on the numerical aperture of the optical fiber, the small signal suddenly increases by around one order of magnitude at threshold; this is the no considered step in the curve that describes the behavior. In this work, we define a Raman generator coefficient (R_{GC}) that allowed us to approximate the theoretical model to the experimental behavior right at the threshold. By considering the R_{GC}, allows us to better understand the physical phenomenon under study.

2.2 Introduction

Stimulated Raman scattering (SRS) in glass fibers was first observed by Stolen *et al.* in 1971 [42] and a year later, one of the parameters associated with SRS, such as Raman gain efficiency (g_R), was measured in standard single-mode optical fibers [43]. Since then, several techniques have been used to measure such parameter; for example, optical time-domain reflectometry [44]-[46], measurements of the optical power transferred from a short-wavelength high-intensity pump signal to a longer-wavelength Raman-shifted signal [47], and by analysis of stimulated Raman scattering threshold [28, 36, 48]. Modeling of Raman amplification in optical fibers has been amply reported since the generation of Stokes wave in the wavelength region 1.1-1.7 μm is considered an excellent platform for improving the efficiency of long-range optical communication and also for building Raman-type fiber lasers [49]-[51]. However, modeling has been subject to several assumptions such as the fact that the Raman gain is considered constant at all pump powers, the linear and non-linear terms in the propagation equations neglect the contribution of spontaneous Raman scattering generation as it will be described later on.

The measurement of the Raman gain efficiency in optical fibers can be essential to predict exactly the Raman gain peak for the next n-order Stokes wave of an arbitrary pump wavelength within the transparency window of a silica fiber. In this work, we reconsider the first two assumptions and the physical facts that construct the model. The main motivation is based on the experimental results that always make us conclude that the typical modeling-assumptions do not exactly correspond to the experimental behavior, particularly at the threshold; i.e., the boundary between the linear and nonlinear regimes of Raman scattering in optical fibers.

2.3 Theoretical Analysis

In a very general way, in Chapter 1 we mentioned the propagation equations for Raman scattering along an optical fiber at both directions (forward and backward); and graphically, we showed the response of the Stokes signal as a function of the coupled pump power. In this section, we are going to estimate the Raman gain efficiency (g_R) by means of the analytical solution of the differential equations that govern the stimulated Raman scattering (SRS); and to perform such estimation it is important to consider that, although the forward and backward Stokes output power increase linearly with the pump power, the forward Stokes output power increases faster and overpowers the counterpropagating Stokes component; for this reason, let us assume a system with only forward propagation of pump and the first-order stokes signal propagating along (L [km]) in an optical fiber as shown in Figure 2.1.

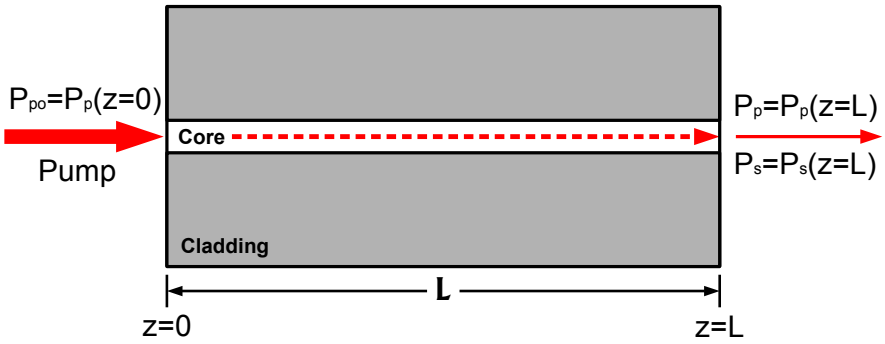

Figure 2.1: Forward propagation in silica fiber

By considering only forward propagation, since P_b is weaker than P_s ($P_s > P_b$), equations (1.14) and (1.15) can be rewritten as follows:

$$\frac{dP_p}{dz} = -\alpha_p P_p - \frac{\lambda_s}{\lambda_p}\frac{g_r}{A_{eff}} P_p P_s \tag{2.1}$$

$$\frac{dP_s}{dz} = -\alpha_s P_s + \frac{g_r}{A_{eff}} P_p P_s \tag{2.2}$$

Where P_p is the pump signal power [W], P_s corresponds to the Stokes signal power [W], λ_p and λ_s are the wavelengths [nm] of the pump and Stokes signals respectively, g_r is the Raman gain term [km/W], and $A_{eff} = \pi w_0^2$ is the effective area [km^2] of the fiber core. At low pump powers $P_s = 0$; hence, only the term of equation (2.1) that contains the attenuation coefficient (α_p [km^{-1}]) contribute to the analysis and the solution of the differential equation from z=0 to z=L is:

$$P_p = P_{po}\, e^{-\alpha_p L} \tag{2.3}$$

Where P_{po} is the coupled input pump power. Let's see the behavior of P_p as a function of P_{po} and of fiber length (Nufern 980-HP of 1-km), with $\alpha_p = 0.3454$ [km^{-1}].

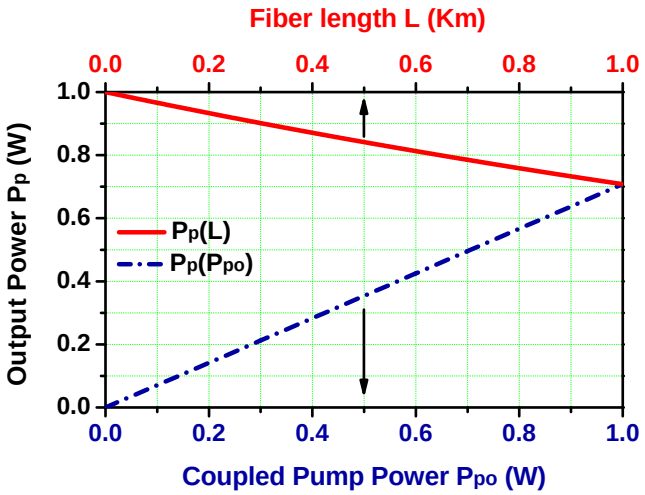

Figure 2.2: Behavior of P_p as a function of coupled pump P_{po} (dashed blue line) and behavior of P_p as a function of fiber length (solid red line), with $\alpha_p = 0.3454$ [km^{-1}].

From equation (2.3), we can express the transmittance as follows:

$$T = \frac{P_p}{P_{po}} = e^{-\alpha_p[km^{-1}]L} = 10^{\frac{-\alpha_p[dB/km]L}{10}} \tag{2.4}$$

So, if we know the powers and we make $\ln T = -\alpha_p[km^{-1}]L$, we obtain:

$$\alpha_p[km^{-1}] = -\frac{1}{L}\ln T \tag{2.5}$$

Or expressed in decibels, we have:

$$\alpha_p[dB/km] = -\frac{10}{L}\frac{\ln T}{\ln 10} = -\frac{10}{L}\log T \tag{2.6}$$

Then, the conversion between $[km^{-1}]$ to $[dB/km]$ is:

$$\alpha_p[km^{-1}] = \frac{\ln 10}{10}\,\alpha_p[dB/km] \approx 0.23026\,\alpha_p[dB/km] \tag{2.7}$$

Note that within the transparency windows of the losses spectrum of silica fiber $\alpha_p \approx \alpha_s$, then it is possible to establish $\alpha = (\alpha_p + \alpha_s)/2$. This approximation is useful to solve for $g_R = g_r/A_{eff}$ in the set of equations (2.1) and (2.2) by means of the following procedure proposed in [7]: first, equation (2.1) is divided by equation (2.2) to obtain equation (2.8).

$$\frac{dP_p}{P_p}\left[-\alpha + \frac{g_r}{A_{eff}}P_p\right] = \frac{dP_s}{P_s}\left[-\alpha - \frac{\lambda_s}{\lambda_p}\frac{g_r}{A_{eff}}P_s\right] \tag{2.8}$$

By solving the second term on the right side of equation (2.2) and substituting it in equation (2.1), we obtain equation (2.9).

$$\frac{d}{dz}\left[\frac{\lambda_p}{\lambda_s}P_p + P_s\right] = -\alpha\left[\frac{\lambda_p}{\lambda_s}P_p + P_s\right] \tag{2.9}$$

Considering that the pumping intensity moves within the silica fiber from z = 0 to z = L, the solution to the differential equation (2.8) is:

$$\ln\left[\frac{P_s P_{po}}{P_{so} P_p}\right] = \frac{\lambda_s}{\lambda_p}\frac{g_r}{\alpha A_{eff}}\left[P_{so} + \frac{\lambda_p}{\lambda_s}P_{po} - \left(P_s + \frac{\lambda_p}{\lambda_s}P_p\right)\right] \tag{2.10}$$

In parallel, the solution to the differential equation (2.9) is:

$$P_s + \frac{\lambda_p}{\lambda_s}P_p = \left[P_{so} + \frac{\lambda_p}{\lambda_s}P_{po}\right]e^{-\alpha z} \tag{2.11}$$

Substituting equation (2.11) in equation (2.10) gives equation (2.12):

$$\ln\left[\frac{P_s P_{po}}{P_{so} P_p}\right] = \frac{\lambda_s}{\lambda_p}\frac{g_r}{A_{eff}}\left[\left(P_{so} + \frac{\lambda_p}{\lambda_s}P_{po}\right)\left(\frac{1-e^{-\alpha z}}{\alpha}\right)\right] \tag{2.12}$$

Where P_{so} is the Raman scattered signal (RS) at the end of the fiber (in z = 0). It is worth noting that RS is the seed for the growth of the Stokes signal. There is an effective length (L_{eff}) that represents the exact interaction length of the pump and the Stokes signals [52], given by:

$$L_{eff} = \frac{1-e^{-\alpha z}}{\alpha} \tag{2.13}$$

Substituting equation (2.13) in equation (2.12), we have:

$$\ln\left[\frac{P_s P_{po}}{P_{so} P_p}\right] = \frac{\lambda_s}{\lambda_p}\frac{g_r}{A_{eff}}\left[\left(P_{so} + \frac{\lambda_p}{\lambda_s}P_{po}\right)L_{eff}\right] \tag{2.14}$$

Ignoring P_{so} in the second member of equation (2.14) for the reason that $P_{so} \ll \frac{\lambda_p}{\lambda_s}P_{po}$ [7], a simple equation that describes an exponential energy transfer from pump power to Stokes power is obtained:

$$g_R = \frac{g_r}{A_{eff}} = \ln\left(\frac{P_s}{P_{so}}\frac{P_{po}}{P_p}\right)\frac{1}{P_{po}L_{eff}} \tag{2.15}$$

Equation (2.15) can be re-written to the form:

$$P_{so} = \frac{P_s P_{po}}{P_p}\, e^{-g_R P_{po} L_{eff}} \tag{2.16}$$

At the threshold, $P_{so} = P_s$. Here one may conveniently consider both linear and nonlinear behavior. Let us consider linear and use equations (2.3) and (2.16) together with the transmittance, $T = P_p/P_{po}$ as follows:

$$e^{-g_R^{th} P_{po}^{th} L_{eff}} = e^{-\alpha_p L} \tag{2.17}$$

That rearranged gives the Raman gain efficiency at the threshold, that is:

$$g_R^{th} = \frac{\alpha_p L}{P_{po}^{th} L_{eff}} \tag{2.18}$$

When $P_s = P_p$, the system reaches the critical power. Therefore, from equation (2.15), we can quantify the Raman gain efficiency with the following relationship:

$$g_R^{cr} = \ln\left(\frac{P_{po}}{P_{so}}\right)\frac{1}{P_{po}^{cr} L_{eff}} \tag{2.19}$$

2.4 Experimental Setup

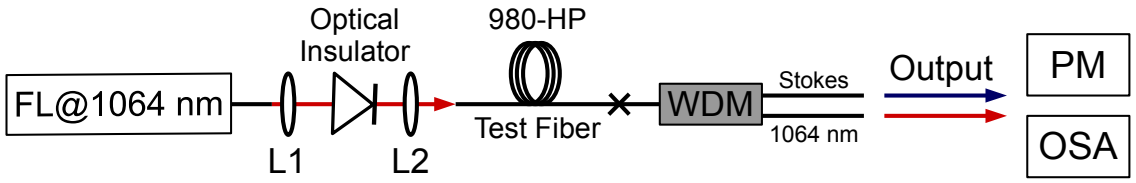

Figure 2.3: Schematic representation of the experimental setup. FL (Fiber Laser), WDM (wavelength-division multiplexer), SMF (single-mode fiber), OSA (Optical Spectrum Analyzer).

Figure 2.3 shows the free-running experimental setup used to characterize the Raman scattering in a single-mode Nufern 980 HP® silica fiber of 1-km when pumping with a 1064-nm ytterbium CW fiber laser (FL-IPG photonics®) delivering up to 10 W. The fiber under test (980-HP), with a ∼3.6 μm-core diameter, was characterized at 1064 nm to have an attenuation of 1.5 dB/km (0.3454 km^{-1}) and by extrapolating to the Stokes signal at 1115 nm [11] we obtain 1.265 dB/km (0.2913 km^{-1}). The pumped fiber was optically isolated from the pump laser to cancel mutual perturbations; also the optical cavity formed by the cleaved ends was reduced by fusion splicing short pieces of multimode fiber (core diameter ∼64 μm and length $<$ 350 μm) that minimized Fresnel reflections [12]; under these conditions stability in the system was assured. To increase the dynamic range of the optical spectrum analyzer (OSA Thorlabs OSA 203®), with resolution manually set at 0.1 nm, we attenuated the pump power by using a characterized WDM device that mainly transmitted the Stokes signal, and supported ∼1.5 watts of power. This was especially important at around the pump threshold where stokes signals are practically negligible compared to the pump. This device delivered the power signals to the OSA that alternatively changed to an optical power meter (PM SOLO-PE form GENTEC-EO®) to measure the average power of the mixed signals.

2.5 Results

Figure 2.4 shows the spectra of four delivered pump powers when they were close to the threshold. From the difference in dBm, one obtains the ratio output (residual) pump to stokes signal [36], hence

$$\frac{P_{so}}{P_p} = 10^{-\frac{\Delta Power(dBm)}{10}} \tag{2.20}$$

Where $\Delta Power = P_p - P_{so}$, when RS just appears at the output. From Figure 2.4, at $P_{p_0} = 1.59$ W (black solid line in the linear regime, below threshold), the residual

pump power is $P_p = 24$ dBm at a maximum level whereas the produced, coupled, and guided, spontaneous Raman signal at the fiber end presents a maximum level of $P_s =$ -30 dBm; then $\Delta P_{wr} = 54$ dB when substituted on equation (2.20) and using equation (2.3) for determining $P_s = P_p \times 10^{-5.4} = 1.59W \times e^{-0.3454} \times 10^{-5.4} = 4.481 \times 10^{-6}W$. This corresponds to the spontaneous signal produced by 1 km of fiber and 1.59 W of pump power.

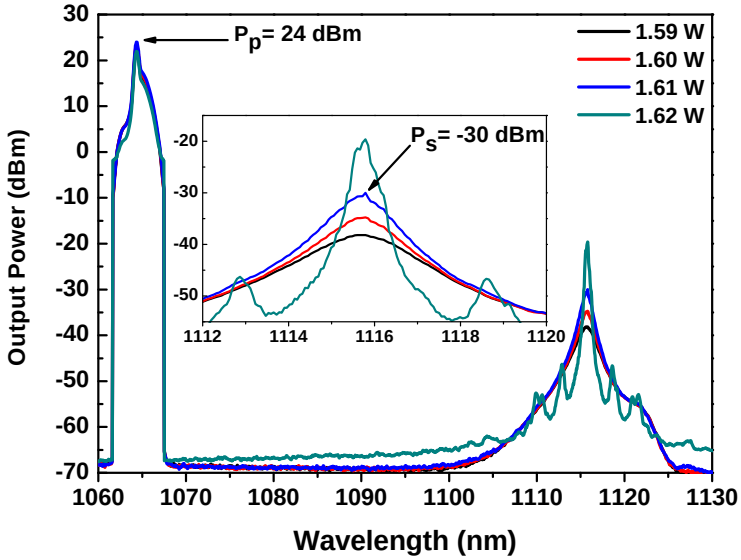

Figure 2.4: Intensity spectra corresponding to four different pump powers for 1-km Nufern 980-HP silica fiber. The resolution of the OSA was manually set at 0.1 nm.

To calculate the spontaneous signal produced by certain pump power and at certain fiber length let us analyze as follows. As the pump power is variable along the optical fiber according to equation (2.3), it is more convenient to consider the average pump power along the optical fiber as follows:

$$P_p^{avg} = \frac{P_{p0}}{L} \int_0^L e^{-\alpha_p l} dl = \frac{P_{p0}}{L} L_{eff} \tag{2.21}$$

Then 1.59 W pump power multiplies $L_{eff} = 0.8455$ km (using α_p) obtaining $P_p^{avg} =$ 1.34 W that produced $P_s = P_{s_0} = 4.481$ μW; then an average power of 1 W through our 1-km fiber produces 3.333 μW of Raman signal. From this analysis, we define a spontaneous Raman generating coefficient $R_{GC} = 3.333 \times 10^{-6}$ km^{-1} that might be included as part of an additional term that modifies the propagation equation (2.2) to

$$\frac{dP_s}{dz} = -\alpha_s P_s + \frac{g_r}{A_{eff}} P_p P_s + R_{GC} P_p \tag{2.22}$$

Then equations (2.1) and (2.22) can be used to model the evolution of both signals along the optical fiber. An important aspect of this is that the Raman spontaneous

is

$$P_s = R_{GC} P_p^{avg} L = R_{GC} P_{p_0} L_{eff} \tag{2.23}$$

There is a group of signals produced at pump levels corresponding to the linear/nonlinear boundary where the Raman signal band becomes evidently narrower; i.e., amplification of Raman signals occurs; this is the stimulated Raman scattering (SRS). In our case occurs at 1.61 W, having $P_p^{avg} = 1.36$ W that produced $P_s = P_p \times 10^{-5.4} = 1.61 \text{ W} \times e^{-0.3454} \times 10^{-5.4} = 4.537 \times 10^{-6}$ W; then an average power of 1 W through our 1-km fiber produces 3.333 μW of Raman signal; having a stimulated Raman generating coefficient $R_{GC} = 3.333 \times 10^{-6}$ km^{-1}. In our case $P_s = 4.537$ μW; as a matter of fact, this is the small-signal that together with the phonons start an aggressive self-nurturing behavior by snatching energy from the pump signal; i.e., the amplified SRS process takes place.

In Figure 2.5 we show the accumulation of Stokes signal along the fiber kilometer for two different coupled pump powers (1 and 1.61 W).

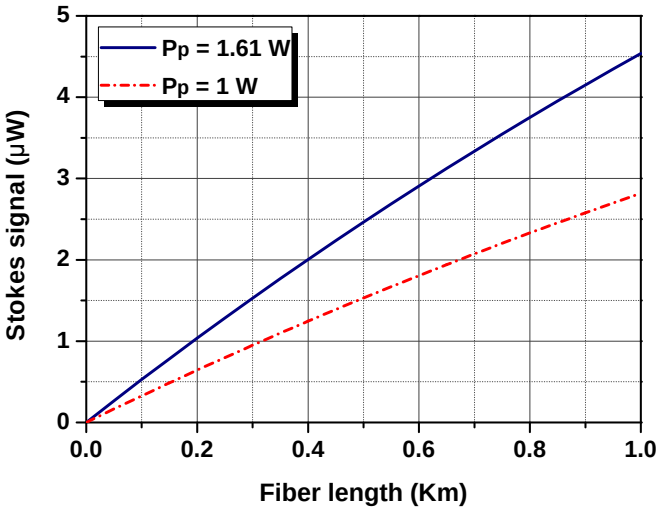

Figure 2.5: Accumulation of Stokes signal in 1-km of fiber with 1 and 1.61 W of coupled pump powers.

In Figure 2.5, it is evident that the Stokes signal adopts magnitudes that from a practical point of view can be negligible; in fact, this has happened in previous studies, but it is important to highlight that these Stokes components are fundamental in the amplification process because they are the seed that will demand pumping energy when the system reaches the operating threshold.

All the spectra obtained from a few pump-coupled milliwatts to several Watts (included the ones from Figure 2.4) were processed to assign the power corresponding to each component as follows. The total area (A_T) under the OSA's spectrum curve covering both signals was calculated and related to the total power (P_T) measured

by the PM. Then, such power was divided according to the area of each spectral component. For example, for a coupled pump power of 2,12 W, the Stokes power (P_{st}) and residual power (P_{re}) were calculated by the following relationships.

$$P_{St} = \frac{A_{St}}{A_T} \cdot P_T \tag{2.24}$$

$$P_{re} = \frac{A_{re}}{A_T} \cdot P_T \tag{2.25}$$

where A_T = Stokes area (A_{st}) + residual area (A_{re}), see Figure 2.6

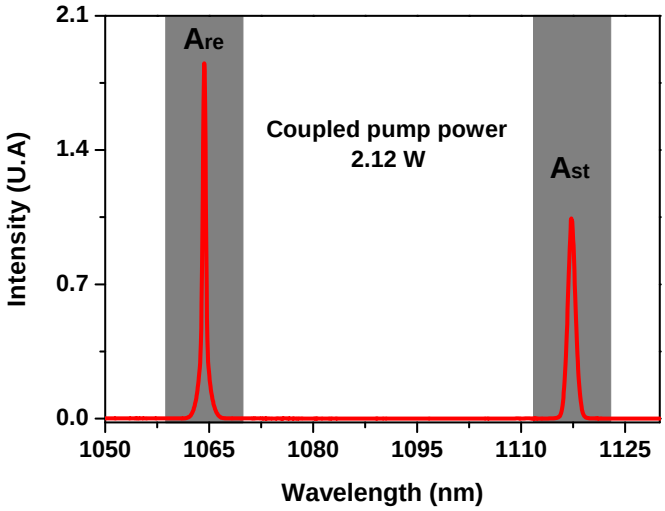

Figure 2.6: Spectrum delivered with a coupled pump power of 2.12 W. The gray-shaded regions are the Stokes (A_{St}) and residual pump (A_{re}) areas.

Figure 2.7 presents such delivered powers as a function of coupled pump power.

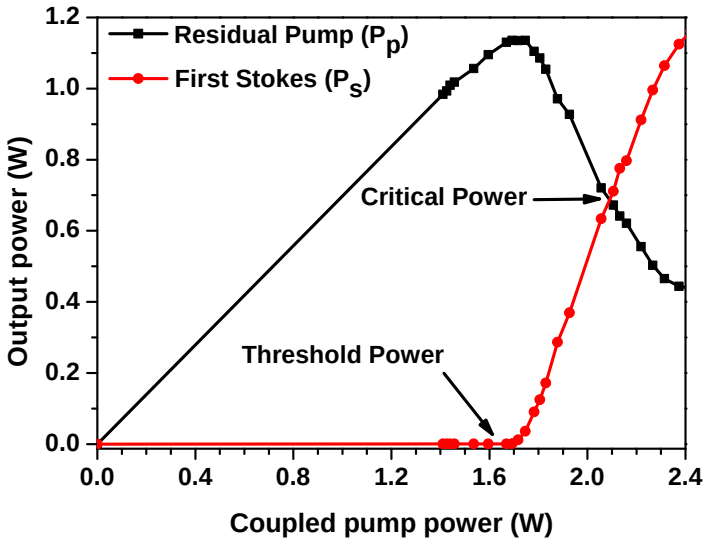

Figure 2.7: Residual pump power and Stokes power at the end of 1-km of Nufern 980-HP silica fiber.

Note that if we do not consider the contribution of the Stokes signal, or if we only consider an average value of it, when modeling the evolution of the residual pump (P_p) and the first Stokes (P_s) as a function of the coupled pumping power, the threshold theoretical does not exactly correspond to the experimental threshold as shown in Figure 2.8.

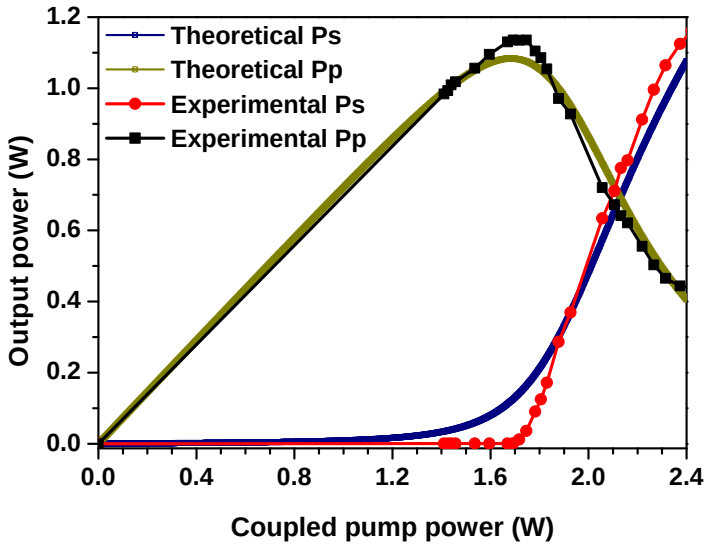

Figure 2.8: Theoretical model versus experimental behavior of Raman amplification neglecting the small Stokes signals.

Focusing on the threshold of Figure 2.8, the theoretical model of P_s indicates that Raman amplification takes place at a much lower coupled-pump power than described in the experimental data. On the other hand, when we take into account the small Stokes signal and consider the $g_R = 1.24$ km^{-1}W^{-1}, the theoretical model is close to the experimental behavior, particularly at the threshold as observed in Figure 2.9.

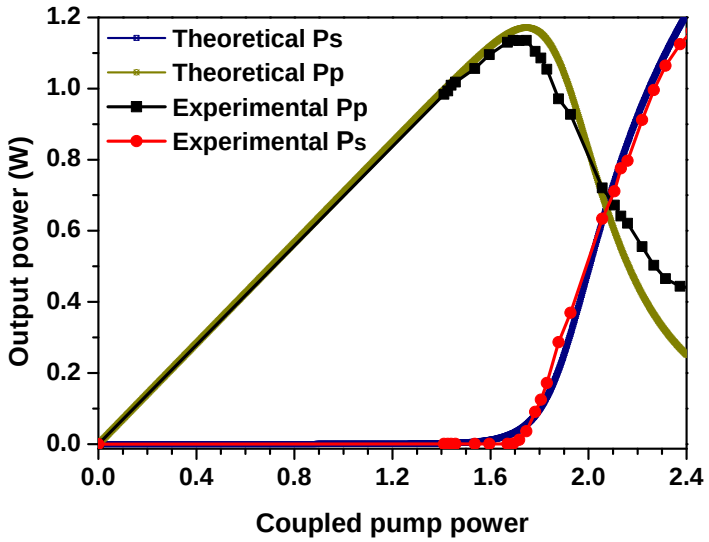

Figure 2.9: Theoretical model versus experimental behavior of Raman amplification considering the small Stokes signals.

Note that the theoretical behavior of P_s at the threshold indicates that the Stokes signals play an important role in the Raman generation; hence, it should not be neglected in the mathematical models that describe this phenomenon.

Finally, another important aspect of our investigation is the fact that the Raman gain efficiency ($g_{_R}$), when modeling Raman laser systems, is considered as a constant. To clarify this, let us now calculate its value at several points. First we use equation (2.13) with $\alpha = 0.31845$ km^{-1} to obtain $L_{eff} = 0.8564$ km; then from Figures 2.4 and 2.7 the threshold pump power $P_p^{th} = 1.61$ W and then from equation (2.18) we obtain the Raman gain efficiency of $g_R^{th} = 0.231$ km^{-1}W^{-1}. Besides, from Figure 2.7, at the critical power ($P_{po} = P_{cr} = 2.12$ W) both, the residual pump and the Stokes, present the same power ($P_p = P_s \approx 0.7$ W). Then using equation (2.15) we obtain $g_{_R}^{cr} = 7.02$ km^{-1}W^{-1}. For 2.4 W pump power $P_s \approx 1.12$ W and $P_p \approx 0.44$ W, thus $g_{_R} = 6.66$ km^{-1}W^{-1}. Note that the maximum Raman gain value is recorded at the critical power.

2.6 Conclusion

We define and quantify a spontaneous Raman generator coefficient (R_{GC}) that, together with the coupled pump power along the fiber, produces the seed that induces Raman amplification when the system reaches the threshold. Considering this small seed, we were able to approximate the theoretical model to the experimental behavior, particularly at the threshold, with greater accuracy than the previously established models. On the other hand, We show that the Raman gain efficiency ($g_{_R}$) is a parameter that varies as a function of the Stokes amplification; i.e., it cannot be considered as a term that operates with the same magnitude for any coupled pump power.

Chapter 3

Active centers as dopants in optical fibers

3.1 Introduction

Rare-earth elements include the 15 lanthanides: Lanthanum (La), Cerium (Ce), Praseodymium (Pr), Neodymium (Nd), Promethium (Pm), Samarium (Sm), Europium (Eu), Gadolinium (Gd), Terbium (Tb), Dysprosium (Dy), Holmium (Ho), Erbium(Er), Thulium(Tm), Ytterbium (Yb), and Lutetium (Lu). Over the past few decades, rare-earth ions doped materials are playing a fundamental role in the field of lasers, fiber amplifiers, sensors, and solid-state lighting devices [53]-[55]. Among all these applications, rare-earth-doped fiber-optic lasers have drawn much attention due to the enormous qualities they offer [56]. To study the characteristics of rare-earth-doped fiber lasers and amplifiers it is important and necessary to understand the spectroscopic properties of their 3^+ ionized state when immersed in glass materials. Rare-earth have important characteristics that distinguish them from other optically active ions. Among these, it stands out that the lifetimes of the meta-stable states are relatively long, and the quantum efficiencies tend to be high [57]. These properties make rare-earth ions excellent candidates for various optical applications [58].

When a glass is doped with active centers such as rare-earths, the atoms use three electrons (e^-) from its outermost shell to bond with the atoms of the material [59]. The unbalance of charges produced by the absence of electrons causes the atoms to ionize, acquiring a 3^+ ionization state. On the other hand, vitreous media are brought to this state from crystals. The most common glass used to make active optical fibers is silica (SiO_2). In its pure form, silica is crystallized and is called quartz. Quartz is made up of a series of unit cells that comprise a few molecules of silica. In turn, the unit cells are perfectly arranged (linked together) to form a solid whose properties are different at different points and in different directions. When the quartz melts, the atoms temporarily release their electrons that form the bonds and when they very

slowly cool down, they recover them and the crystals are formed again. However, if the crystal does not have enough time to regain its natural shape; i.e., if it cools faster, the unit cells are distorted and the perfectly ordered arrangement no longer takes place. Then it can be said that the crystal stopped in the glassy phase that implies loss of anisotropy to become isotropic[1].

The triply ionized rare-earths change or acquire absorption and emission properties, as well as lifetimes of the excited states, depending on the material in which they are immersed [60].

3.2 Triply ionized rare-earths as active centers

Atoms consist of neutrons and protons found in the nucleus and electrons found in orbitals in radial space outside the nucleus. The energy of each electron is defined by four quantum numbers (n, l, m, s) as follows. In the simplest atom (hydrogen), the only electron is found within a certain radial region that is defined by a quantum number (n). This electron has a value n = 1 which is the region or shell closest to the nucleus. The shape of the orbital that this electron occupies is spherical and as such, the angular momentum of the electron is zero ($l = 0$). The third number of the quantum state of this electron refers to the orientation of the orbital or suborbital, which in the spherical case is m = 0; i.e., it has no orientation. Finally, the fourth number that defines the quantum state of the electron is the direction of its rotation about its own axis (Spin), which can have only two values $-1/2$ or $1/2$ [61]. As the number of electrons increases, they occupy the quantum states of the atoms according to a certain order, giving rise to a new chemical element. For example, in the case of Xenon $[^{54}Xe]$ its electronic configuration is: $1s^2 2s^2 2p^6 3s^2 3p^6 4s^2 3d^{10} 4p^6 5s^2 4d^{10} 5p^6$ [62] and its atomic number is 54. This element is taken as a starting point to later describe the electronic configurations of the 15 elements within the rare-earths family; e.g., ytterbium (Yb) is one of the rare-earth belonging to the lanthanide series, its atomic number is 70, and its atomic weight 173.04. The electron configuration of ytterbium is $[^{54}Xe]6s^2 4f^{14}$ [62].

Rare-earth have atomic numbers from 57 to 71 of the periodic table and their electronic configuration is $[^{54}Xe]\ 4f^n$ [62]; from which, 3 electrons of the outermost shell form chemical bonds to the crystalline or glass lattice, so it is positively ionized 3^+ as it is missing 3 electrons. In this way, the first rare-earth, lanthanum $[^{57}La]$ with atomic number 57, acquires a configuration like Xenon $[^{54}Xe]\ 4f^0$ with zero electrons in the next suborbital of the f-type filling order. So, we say that lanthanum is not optically active because it has "closed" shell. The next rare earth is cerium $[^{58}Ce]$

[1] Materials with the same optical properties in all directions

with atomic number 58 and electron configuration $[^{54}Xe]\ 4f^1$. According to its configuration, cerium has a shell "Open" in the sense that the single electron occupying the set of sub-orbitals of shell **f** can easily change its quantum state occupying any other sub-orbital or Spin number. Thus, the rare-earths adopt the form presented in Table 3.1.

Table 3.1: Lanthanide configuration, starting from the Xenon configuration

Name	Symbol	Configuration	Name	Symbol	Configuration
Lanthanum	La^{3+}	$[^{54}Xe]4f^0$	Terbium	Tb^{3+}	$[^{54}Xe]4f^8$
Cerium	Ce^{3+}	$[^{54}Xe]4f^1$	Dysprosium	Dy^{3+}	$[^{54}Xe]4f^9$
Praseodymium	Pr^{3+}	$[^{54}Xe]4f^2$	Holmium	Ho^{3+}	$[^{54}Xe]4f^{10}$
Neodymium	Nd^{3+}	$[^{54}Xe]4f^3$	Erbium	Er^{3+}	$[^{54}Xe]4f^{11}$
Promethium	Pm^{3+}	$[^{54}Xe]4f^4$	Thulium	Tm^{3+}	$[^{54}Xe]4f^{12}$
Samarium	Sm^{3+}	$[^{54}Xe]4f^5$	Ytterbium	Yb^{3+}	$[^{54}Xe]4f^{13}$
Europium	Eu^{3+}	$[^{54}Xe]4f^6$	Lutetium	Lu^{3+}	$[^{54}Xe]4f^{14}$
Gadolinium	Gd^{3+}	$[^{54}Xe]4f^7$			

The rare-earth La^{3+} and Lu^{3+} have closed configurations, the first one does not have electrons in **"f"** that can be excited to occupy vacant quantum states. While, in the second, all states are occupied. The other rare-earth are active. The natural arrangement of electrons in the **"f"** shell results in the rare-earth ground state. These have the energy that corresponds to the vector superposition of all the quantum states of the electrons. Changes in the electronic arrangement of 4**f** imply changes in the ion energy; therefore, the number of possible energetic states that it can take when excited depends on the number of vacant sites; e.g., the Yb^{3+} only has one site available, apart from the base state.

The resulting vector of the angular momentum (vectors of the e^- in the 4**f** shell) is denoted by **L** while the resulting vector of the spin is denoted by **S**. So, the resulting angular momentum of rare-earth is $\mathbf{J} = \mathbf{L} + \mathbf{S}$ [63]. This is known as the Russel-Saunders or spin-orbital coupling because each possible variation of the 4**f** arrangement has its own **J**, **L**, **S** set of values; its energy values are presented as [57]:

$$^{2|S|+1}L_J \tag{3.1}$$

where

$$S = \sum_{i=1}^{n} s_i \qquad ; \qquad L = \sum_{i=1}^{n} \ell_i \tag{3.2}$$

The possible values of **L** are given by the letters (S, P, D, F ...) corresponding

respectively to (0, 1, 2, 3, ...). This makes sense of the labeling of energy levels found in the literature. The term $2|S|+1$ gives information about the spins, **L** about the orbitals and **J** is a combination of both. Although very complicated for most rare-earth, let us look at the simplest example which is Ytterbium Yb^{3+}. Its **J**, **L**, **S** values are:

$$S = \sum_{i=1}^{n=1} s_i = \pm\frac{1}{2} \qquad ; \qquad L = \sum_{i=1}^{n=1} \ell_i = 3 \tag{3.3}$$

The term n = 1 indicates that there is a single-electron Spin and L = 3 is the single-electron F-type orbital. From the above, we have that the base state of Ytterbium is given as follows:

$$^{2|\frac{1}{2}|+1}F_{3+\frac{1}{2}} =^2 F_{\frac{7}{2}} \tag{3.4}$$

While the excited state of Ytterbium has the following expression:

$$^2F_{3-\frac{1}{2}} =^2 F_{\frac{5}{2}} \tag{3.5}$$

3.3 Optical properties of rare-earths in glasses

As mentioned, rare-earths have their free-state energy level systems well established; however, since they are immersed in a solid-state (glass-crystals) and interact with the electrostatic fields of the network, their level system undergoes a splitting that generates sub-levels. This multiplier effect of energy levels is called the **Stark effect**. Therefore, the original levels are broken down into sets of sub-levels that are separated from a few tens to a few hundred cm^{-1}. In the simplest case, which is triply ionized Ytterbium (Yb^{3+}), its base and excited state decompose into 4 and 3 sub-levels respectively, which for this case are obtained by adding **J**+**S** at each energy level.

Therefore, for the base state J=$\frac{7}{2}$ and S=$\frac{1}{2}$ which indicates that the number of Stark levels is equal to 4. For its part, for the excited state J=$\frac{5}{2}$ and S=$\frac{1}{2}$ which indicates that the number of Stark levels is equal to 3 [64]. Due to the above, ytterbium-doped silica fibers can be pumped with a wide range of wavelengths to produce other wavelengths of general interest. Hence, the (Yb^{3+}) with all its levels and sub-levels is as shown in Figure 3.1. The meaning of energy in cm^{-1} is that a certain number of wavelengths fits in 1 cm as follows:

$$E[cm^{-1}]\lambda = 10^{-2} \tag{3.6}$$

For example, for E = 600 cm^{-1} we have $\lambda_{(photon)} = 10^{-2}m/600 = 16.6\mu m$. Other

relations to describe the energy of photons are: E[J] = hν = $\hbar w$ which corresponds to the energy in Joules with frequency ν; y E[eV] = $\frac{h\nu}{1.6}10^{19}$ eV corresponding to the energy in electron-volts.

It is worth noting that, with increasing temperature, the Yb^{3+} sub-levels tend to widen and overlap at room temperature, forming energy bands. The ions in a crystal are subjected to an identical electrostatic environment due to the ordered atoms. In this way, all ions have the same Stark splitting and therefore a homogeneous broadening is said to exist. In the case of a glass, each ion has its own Stark sub-level system because its environment is unique due to the distribution of distorted unit cells. Then it is said that, in a glass, a rare-earth population undergoes (*in general*) an in-homogeneous broadening [63].

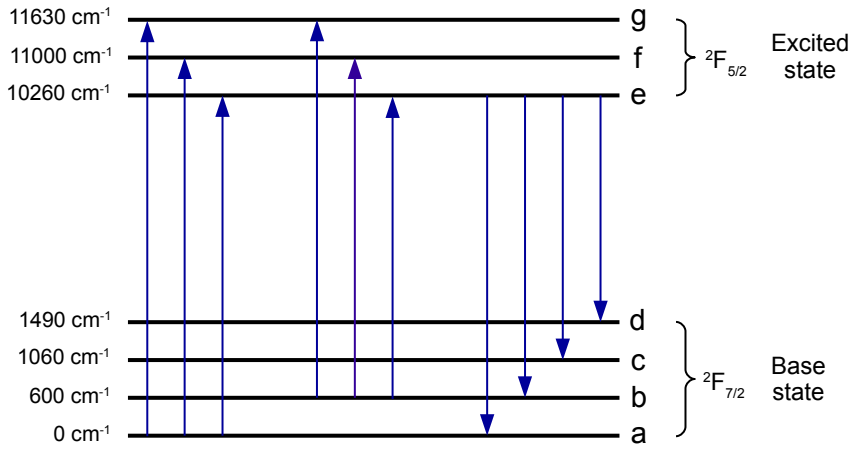

Figure 3.1: Energy levels for Yb^{+3} in glass or crystal at cryogenic temperature ($0^oK \approx -273^oC$)

Dopant-free glasses respond differently to temperature depending on the size of their molecules. In general, most glasses have properties between silica whose molecules are small, and ZBLAN (*Zirconium, Barium, Lanthanum, Aluminum, and Sodium*) with large molecules [65]. In the first of them, the molecular vibrations are distributed in bands that together cover a region of low frequencies (*mechanical*) of up to 49 THz that correspond to a wavelength of the phonon of 7.5 μm in the infrared with $\Delta E \leq 1300$ cm^{-1} (*for all practical purposes, it is considered as 1100 cm^{-1}*) and with a maximum (*overlap of modes*) between 7.5 and 15.5 THz (*with peaks at 13.2 THz and 14.1 THz*) corresponding to 40 and 19.35 μm respectively. In contrast, ZBLAN has a narrower spectrum with its maximum at the highest frequency end of 15 THz corresponding to a phonon wavelength of 20 μm ($\Delta E = 580$ cm^{-1}) [66, 67].

In rare-earth-doped glasses, these vibrational bands widen both the Stark sub-levels and the bands produced by their overlap. This means that there is a tendency for an overlap between nearby energy; when this happens, the radiative transitions

(*emission of photons*) between nearby bands become inhibited and give rise to non-radiative transitions; i.e., the transitions between almost overlapping levels release small energy quanta that are resonant with the vibrational modes of the glass called phonons (*energetic quanta that heat the host material and therefore do not produce radiation*). This type of decay is almost instantaneous compared to the times of photon radiative meta-stable states. See Figure 3.2.

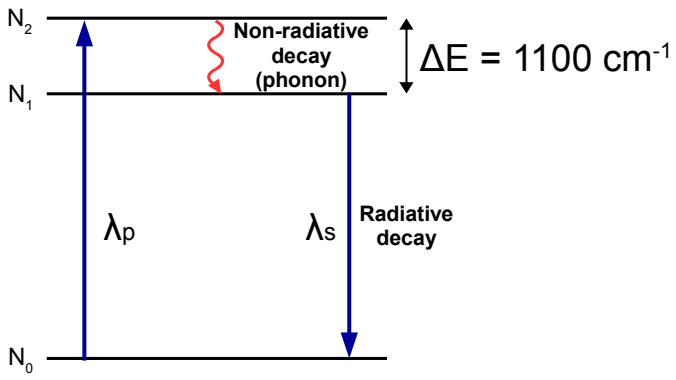

Figure 3.2: Excitation of rare earth in silica. Between the two upper levels, there is only phononic decay

Then, the non-radiative decay lessens the establishment of meta-stable states; e.g., when there are two energy levels (in rare-earth-doped glass) spaced in the order of the silica phonon (see Figure 3.2), the N_2 level instead of decaying to the ground state, decay to N_1 releasing phonons and feeding with high efficiency to N_1. As the energy distance from N_1 to N_0 is greater than $\Delta E = 1100cm^{-1}$ (*typically this value is established as the maximum energy of the* SiO_2 *phonon*), the probability of phononic decay is minimal and photonic decay is prioritized. According to the theory, this type of decay occurs for energies approximately greater than $3\Delta E$. Let's see the previous example for ZBLAN, Figure 3.3.

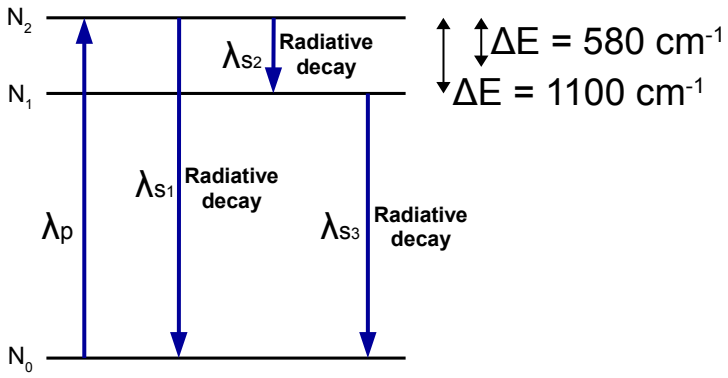

Figure 3.3: Rare-earth excitation in ZBLAN. Between the upper level and the two lower levels, there is photon decay

In this case, the phononic connection between N_1 and N_2 is less compared to the silica scheme. This means that there is less phononic decay and radiative decays are

favored. So it is said that in ZBLAN the phonons are less energetic and the radiative efficiency is higher. This produces an increase in the number of transitions that fluoresce due to an increase in their lifetime. It can then be said that materials whose phonons are less energetic present more metastable states and therefore behave with ***"greater richness"*** in the sense that they present more luminous transitions. This greater disconnection between transitions, through phonons, increases the lifetimes of the excited levels in ZBLAN-like materials such as Tellurium.

3.3.1 Absorption and emission spectra of rare earths in glasses

Every absorption band, of rare-earth immersed in glass, has an associated emission band slightly shifted to the infrared (IR). The mathematical relationship between these bands has been established by *McCumber* [68].

$$\sigma_{emi}(\lambda) = \sigma_{abs}(\lambda) e^{\frac{\epsilon - h\nu}{KT[^oK]}} \tag{3.7}$$

Where ϵ is the energy difference between the levels at cryogenic temperature (*very low temperatures*), **k** is the Boltzman constant ($1.38 * 10^{-23} \frac{J}{^oK}$), **T** is the temperature in ^oK and **h** is Planck's constant ($6.626 * 10^{-34} JS$). Another form of this relationship is:

$$\sigma_{emi}(\lambda) = \sigma_{abs}(\lambda) e^{\frac{hc}{KT[^oK]}(\frac{\lambda - \lambda_0}{\lambda\lambda_0})} \tag{3.8}$$

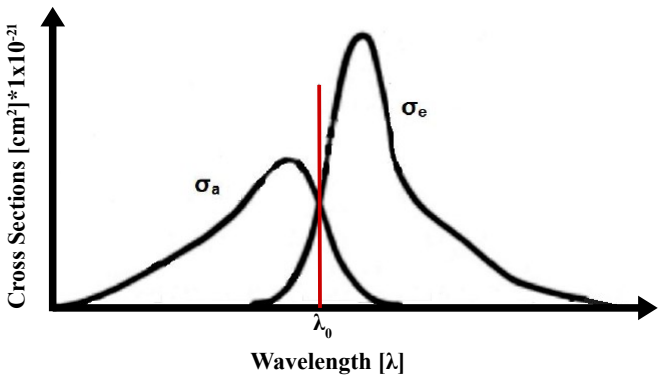

Figure 3.4: Location of λ_0 in absorption and emission cross-section

Where λ_0 is the wavelength at which the emission and absorption cross-sections coincide (Figure 3.4), and can be obtained from [69]:

$$\lambda_0 = \frac{10^{-2}}{\Delta E[cm^{-1}]} \tag{3.9}$$

3.4 Absorption in passive-active media

Optical fibers can usually operate as an attenuating or amplifying means. Its nature, in the linear regime; i.e., when they guide moderate intensities, their tendency is to

attenuate. However, by introducing dopants and activating them, they become active centers that play the role of counteracting attenuation. The balance between these two parameters tells us whether an optical fiber attenuates, amplifies, or is simply transparent. When doping an optical fiber with active centers that can generate amplification and when pump it, its losses behave according to the pump power level as expressed in the following relationship:

$$\alpha_p(P_p) = \alpha_o + \frac{\alpha_{po}}{1 + \frac{P_p}{P_p^{sat}}} \tag{3.10}$$

Where P_p is the pump power, α_o is the intrinsic loss constant of the glass described in the previous section, P_p^{sat} is the saturation pump power and α_{po} are the small-signal losses of the pump produced by dopants. In this sense, it is established that $\alpha_{po} > \alpha_o$ and therefore the following relationships are generated:

$$\alpha_{po} = \sigma_{abs} N_o \tag{3.11}$$

$$P_p^{sat} = \frac{h\nu_p a}{\sigma_{abs}\tau} \tag{3.12}$$

From relationship 3.11, absorption sigma (σ_{abs}) is the cross-sectional area analogous to the absorption capacity of the active center as a function of wavelength, its unit is $[m^2]$; (N_o) is the volumetric density of dopants given in numbers of dopants per unit volume $[centros/m^3]$; and from relationship 3.12, (h) is Planck's constant (6.626×10^{-34} Js), here (a) is the cross section area of the fiber core and (τ) is the time that excited dopants remain before decaying spontaneously (lifetime of the excited state). For quasi two-level systems, it is necessary to take into account that the pump signal has components σ_{abs} and σ_{emi}; e.g., ytterbium pumped at 976 nm. Then we can express P_p^{sat} as

$$P_p^{sat} = \frac{h\nu_p a}{[\sigma_{abs}(\lambda_p) + \sigma_{emi}(\lambda_p)]\tau} \tag{3.13}$$

Where σ_{emi} is the opposite of σ_{abs} as shown in section 3.5 (Absortion in pumped active media).

3.4.1 Small signal regime (passive)

When the pump power is very low (practically zero) we have:

$$\alpha_p(0) = \alpha_o + \alpha_{po} \tag{3.14}$$

Whereas when we increase the pump power to the value $P_p = P_p^{sat}$ we obtain

saturation of the system, which is when the second term falls by half, that is:

$$\alpha_p(P_p = P_p^{sat}) = \alpha_o + \frac{\alpha_{po}}{2} \tag{3.15}$$

3.4.2 Large signal regime (active)

When the pump signal exceeds the saturation power P_p^{sat}, the center begins to respond actively and at the limit where it exceeds the saturation pump power, the power-dependent loss reaches zero, then:

$$\alpha_p = (P_p >> P_p^{sat}) = \alpha_0 \tag{3.16}$$

The result is practically the fading or disappearance of the absorption by dopants; i.e., the dopants become transparent for very intense pumps. It is possible that there are clusters of 2 or 3 ytterbium ions that can each absorb a pump photon and double or triple the emission frequency, and this may correspond to the addition of a third term in the total loss equation of the active medium. There is also the possibility, supported by some authors, that the blue-green emission may also be due to the presence of an impurity of thulium ions that absorb with great efficiency both the pumping (976 nm) and the emission of ytterbium; thus generating, by the upconversion phenomenon, the absorption of several infrared photons to emit a higher frequency photon. We even observed that with very high pump power of 976 nm, red, blue and orange-yellow components appeared, transitions that may correspond to emission by upconversion of the thulium ion; or as emissions produced by clusters of 3 or more ytterbium ions.

3.5 Absorption in pumped active media

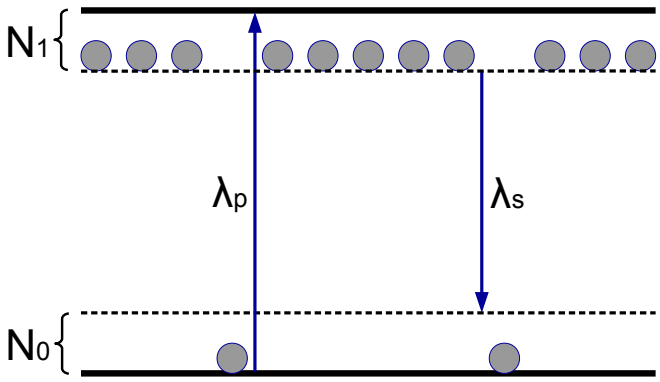

Figure 3.5: 2-level diagram of active centers

When an active medium is sufficiently pumped, the active centers are energy redistributed, some of them remaining at the highest energy levels, while others remain at the base level. In a simplified two-level scheme, the active centers that are excited at

the highest level tend to lodge in the lower part of said level, those that remain in the ground state agglomerate in the lower part of it. In this way, it can be assumed that between the lower part of the upper band (level) and the upper part of the base state the condition called population inversion is established as illustrated in Figure 3.5.

The loss of a small signal at λ_s in a sufficiently pumped medium would be:

$$\alpha_s(P_s \approx 0) = \alpha_{so} = \alpha_o + \sigma_{abs}N_o - \sigma_{emi}N_1 \tag{3.17}$$

Since $N_1 >> N_0$ then for a medium with a very low intrinsic loss α_0, we have:

$$\alpha_{so} = \alpha_o - \sigma_{emi}N_1 \approx -\sigma_{emi}N_1 \tag{3.18}$$

The negative sign indicates an amplification because $(\sigma_{emi}N_1)$ is a loss. In this sense, the negative sign of this absorption coefficient implies a process opposite to absorption, which is gain. In this way, we can rename it with the small-signal gain coefficient as follows:

$$g_o = \sigma_{emi}N_1 \tag{3.19}$$

So, in a doped optical fiber, we have a small-signal net gain as follows:

$$g_{net}(0) = g_o - \alpha_o = \sigma_{emi}N_1 - \alpha_o \tag{3.20}$$

Where σ_{emi} is the opposite analog of σ_{abs}; i.e., when we had the product $N_0\sigma_{abs}$ we assumed a small area σ_{abs} multiplied by N_0 times; on the contrary, the product $N_1\sigma_{emi}$ would have the physical meaning of an emitting area that would be σ_{emi} multiplied by N_1 times.

In the case of gain, there is also a saturation threshold for that; then, there is also a power that the signal must have so that the gain "falls" by half. Thus, we define a saturation signal power as shown by the following relationship:

$$P_s^{sat} = \frac{h\nu_s a}{\sigma_{emi}\tau} \tag{3.21}$$

Once again, it is necessary to take into account that the signal has components σ_{abs} and σ_{emi}; therefore, we can express P_s^{sat} as

$$P_s^{sat} = \frac{h\nu_s a}{[\sigma_{abs}(\lambda_s) + \sigma_{emi}(\lambda_s)]\tau} \tag{3.22}$$

In this way, we are now able to define a net gain whose value depends on the level

(*power*) of the signal given by:

$$g_{net}(P_s) = \frac{g_o}{1 + \frac{P_s}{P_s^{sat}}} - \alpha_o \tag{3.23}$$

Where the first term to the right of the equality sign is the doping gain. So, for a doped and sufficiently pumped optical fiber we have that the transmittance is:

$$T = \frac{P_L}{P_o} = e^{Lg_{net}} \tag{3.24}$$

Therefore, we have that $e^{-\alpha L}$ represents the loss of the signal and $e^{Lg_{net}}$ is the gain of said signal. Finally, we alternatively define the net gain of the active medium as:

$$g_{signal}\left[km^{-1}\right] = \frac{1}{L}\ln T \tag{3.25}$$

This gain can also be defined in dB/m as:

$$g_{signal}[dB/km] = \frac{10}{L}\log T \tag{3.26}$$

Chapter 4

Performance improvements of a hybrid (Raman-Ytterbium) ring fiber laser

4.1 Abstract

This work presents the results and analysis of the modification of a Raman fiber laser (RFL) departing from a simple free-running distributed-feedback configuration that emitted two main wide bands; then it was modified into a ring configuration; after that, a Fabry-Perot filter was inserted; and finally, a piece of Yb^{3+}-doped fiber was spliced into the Raman gain medium to further improve the performance of the system. All modifications contributed to the enhancement the efficiency. In addition, the first one, the modification to a ring cavity, selected one of the two main bands to oscillate; the second one, the one with the Fabry-Perot filter inserted, selected a single-line with high stability to oscillate; and the last, the one with a piece of Yb^{3+}-doped fiber inserted, contributed to decreasing the operating threshold because the amplified spontaneous emission (ASE) from the Yb^{3+} ions forced the stimulated Raman scattering process to initiate earlier. With this last setup: laser emission is stable, less than 1-nm single Stokes line is emitted, the conversion efficiency increase, and the threshold decreased compared to the previous configurations. We propose this hybrid configuration when high stability, high efficiency, and single-line emission is desired in Raman fiber lasers.

4.2 Introduction

Raman fiber lasers (RFLs) use Stimulated Raman Scattering (SRS) to shift the input wavelength (pump signal) to another desired wavelength (Stokes signal). This gain mechanism generates, in most cases, highly efficient sources that cover the near-infrared from around 1000 nm to 1500 nm [70, 71, 72]; and with the proper ar-

rangements, they may also cover the visible when the frequency-doubled [73, 74]. An advantage of RFLs is that all the glass molecules, within the core of the optical fibers, participate in the Stokes amplification process, unlike other fiber lasers limited by the concentrations of dopants [51, 63, 75]. Due to the characteristic of Raman amplification, which can provide in-homogeneous broadened gain bands (by selecting the pump wavelengths) of SRS, it makes RFLs suitable for a wide variety of applications ranging from medical applications, materials processing, terahertz generation, testing-measurement of wavelength division multiplexing (WDM) components, telecommunications [27] and spectroscopy, among many more. With this wide field of applications, several approaches for these kinds of lasers have been investigated and proposed, many of them widely commercialized. The work reported here relies on the hybrid combination of a Raman fiber laser and Yb^{3+}-doped fiber laser operating together, each one contributing with its best attributes, proposing a way to obtain high efficiency, low threshold, single-line emission with high stability in fiber lasers.

As with any fiber laser, RFLs basically consist of a pump source followed by a Raman gain (g_R) fiber (RGF) that provides amplification and an optical cavity that traps the light. In the simplest free-running RFL setup, the Raman-Stokes oscillation takes place within a non-selective cavity whose "broadband mirrors" are composed of the randomly distributed feedback (RDFB) along the entire fiber, as core-coupled Rayleigh scattering. In addition, sometimes there is an additional non-selective contribution of the perpendicular to the fiber axis glass-air interface(s) at the end(s) of the RGF [76]. In a basic setup, the temperature, the characteristics of the fiber, and the absence of a selective cavity give the system a certain degree of freedom to oscillate, making it unstable by the multiple competing signals oscillating. To acquire control of some parameters such as the wavelength(s) desired, stability, and efficiency, some adequations have to be made. One way of controlling the signals inside a broadband laser cavity was reported in [77]; they present an experimental method to control these signals. In that work, they compared a free-running versus ring-cavity setup. With the last setup, the system was more efficient in all respects, the lasing threshold decreased, the Stokes power output increased and the system was more stable. Another method of signals control was reported in [78]; they studied spectral changes produced by a quite simple adjustable intra-cavity Fabry-Perot interferometer (FPI) inserted into a single-end emitting Yb^{3+}-doped fiber laser (YbDFL); with this configuration the pump power threshold decreased but most important, the FPI selected multi- or single-line oscillations. Another configuration inserts a short piece of YbDF inside an RFL cavity, forming a hybrid system [79, 80, 81]. By simultaneously pumping the Raman gain medium and Yb^{3+}-dopants within the laser cavity, the system takes advantage of the amplified spontaneous emission of ytterbium to drastically reduce the oscillation threshold of the Raman generated Stokes components. In this way, the

laser takes advantage of both types of lasers, YbDFL and RFL.

It is worth noting that typically low-oscillation thresholds do not necessarily correspond to high conversion efficiencies, neither the contrary; as a matter of fact, high-Q cavities have low thresholds but because most energy circulates inside the cavities, the efficiencies tend to be modest; by contrary, low-Q cavities present higher thresholds but once they start delivering energy, they deliver great quantities as they have a high output coupler [82]. In this sense, the ideal laser system fulfills both qualities. This is the aim we are pursuing in this work and it is detailed right below.

4.3 Experiments and results

The initial experimental configuration consisted of a free-running RFL of 4.8 km of silica fiber (OFS TrueWave®LS) as the Raman gain fiber (RGF); that was single-mode (SM) from 1250 nm to longer wavelengths, one wavelength-division multiplexers (WDM), and a single-mode variable power (0 - 10 W) YbDFL as a pump source from IPG Photonics® that emits CW at 1064 nm with ∼0.4 nm linewidth. The schematic of this setup is shown in Figure 4.1.

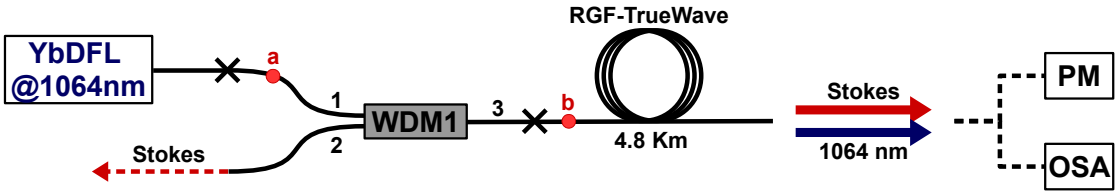

Figure 4.1: Experimental setup of the free-running Raman laser. OSA (optical spectrum analyzer), PM (power meter)

All commercial silica fibers can be considered to function as Raman gain fibers, the parameter that differentiates one fiber from the other is the Raman gain coefficient; i.e., the ability of a given fiber to convert pump power into Stokes power, and this is related to the type of dopant present in the fiber core; e.g., the addition of germanium oxide (GeO_2) in the fibre core leads to an enhancement of the Raman gain coefficient and a reduction of the mode feld radius due to an increased core-cladding index mismatch (thus increasing the power density in the fibre core). As a matter of fact in GeO_2-doped silica fibres the Raman gain coefficient depends linearly on germania con-centration [83] while the Raman gain peak coefficient shifts towards 420 cm^{-1} [84]. The addition of dopant in the fibre inner core leads also to an enhancement of optical losses; for this reason the question of what is the dopant concentration and fibre parameters setting that can offer optimized conversion performances, arises.

To achieve the scheme in Figure 4.1, we start by splicing arm 1 of the WDM1 to the pump laser (YbDFL), and arm 3 was spliced to the 6.5±0.1 μm core diameter RGF. In all configurations, the output end of the fiber was flat ($\backsim$4% reflection). Next, pump power was progressively coupled, to the RGF, until reaching the Raman threshold and the critical power; i.e., where the Stokes power is equal to the pump residual power. At the end of the experimental setup, an optical spectrum analyzer (Thorlabs OSA 203®) with resolution manually set at 0.1 nm, and an optical power meter (PM-SOLO-PE® Model from GENTEC-EO) were alternatively used for the spectral analysis and power measurements of the signals (residual pump and Stokes) delivered.

It is worth noting that the configuration in Figure 4.1 is a non-resonant distributed feedback (DFB) cavity that relies on Raleigh scattered (and core-coupled) Stokes signal along the RGF; in this sense, all the wavelength components within the Stokes become amplified by the stimulated Raman scattering phenomenon and therefore it is a non-selective cavity; although selectivity is usually accomplished by using mirrors or fiber Bragg gratings (FBGs), our approach does not rely on that as described later on.

From here on, when we talk about coupled pump power, we refer to the power delivered in point "b" of the experimental setup. This point is located one meter away from the splice point and right there, at the end of the entire experimental process, the fiber was cut to measure (with the PM) the coupled pump powers in the RGF. Under this clarification, for coupled pump powers below 0.69 W, the system operated in the linear regime; therefore, only residual pump (at 1064 nm) was recorded at the output of the Raman gain fiber as can been seen in Figure 4.2 for a coupled pump power of 0.5 W.

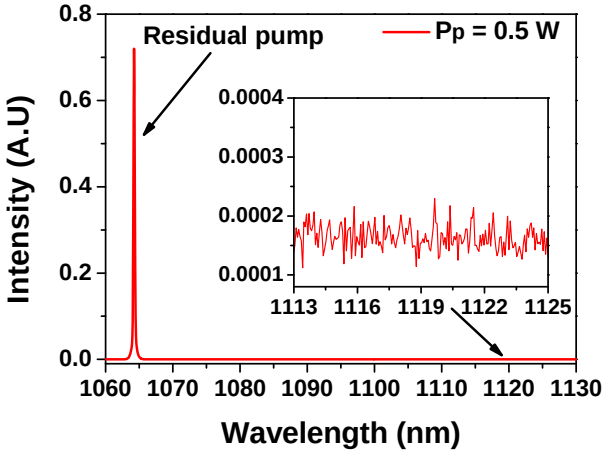

Figure 4.2: Output spectrum for 4% feedback with a coupled pump power of 0.5 W

The inset inside Figure 4.2 magnifies the spectral region (between 1113 - 1125 nm) where amplification of the Rama signal will later take place. Note that at 0.5 W of coupled power, the Stokes component is absent. By increasing the pumping level and

achieving 0.69 W of coupled power, the system reached the Raman emission threshold (first Stokes). This is the limit between the linear and non-linear regime; therefore, the fiber enters a state of transparency because the gain equals the the losses of the fiber, losses that we will be calculated later. Figure 4.3 shows the spectrum recorded by the OSA around the threshold.

Figure 4.3 mainly shows the residual pump at 1064 nm. The inset inside the Figure magnifies the part of the spectrum where the beginning of the energy transfer (Raman threshold) towards the Stokes component is evidenced. Within the main band, centered at 1116.35 nm, three competing laser lines take place at 1116.15, 1116.27, and 1116.46 nm. Note that the residual signal is approximately 2800 times more intense (Peak intensity) than the Stokes component.

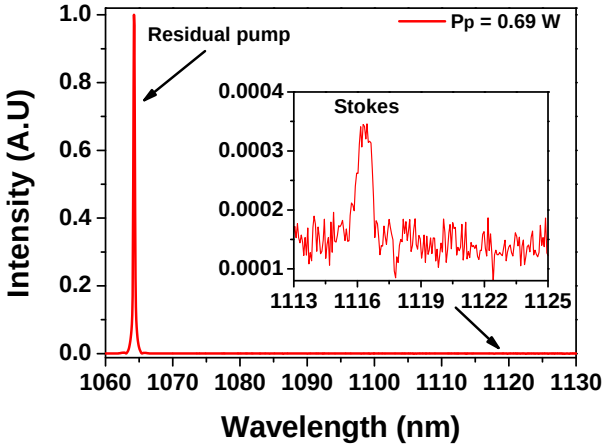

Figure 4.3: Raman threshold at 0.69 W coupled pump power

From here, and for coupled pump powers greater than 0.69 W, the system goes to the non-linear regime, and the energy transfer is even more noticeable with the amplification of the Stokes signals as observed in Figure 4.4 for a coupled pump power of 0.96 W.

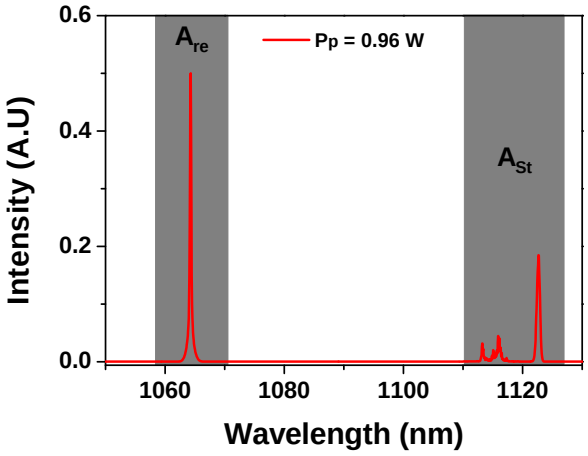

Figure 4.4: Output spectra for 4% feedback. The gray-shaded regions are the Stokes (A_{St}) and residual pump (A_{re}) areas, with coupled pump power (P_p) of 0.96 W.

Since the PM measures all the power discriminating its spectral distribution, the power delivered at each signal, Stokes and residual pump at different coupled-pump powers, was estimated as the quotient of the area under the curve of its spectral profile over the sum of both spectral profiles; all this, multiplied by the power of the mix of signals delivered at the end of the experimental setup. For example, the power of the Stokes signal (P_{St}) is calculated by the following relationship:

$$P_{St} = \frac{A_{St}}{A_t} P_T \tag{4.1}$$

Where total area (A_T) = Stokes area (A_{St}) + residual area (A_{re}), and P_T is the total power measured at the output with the PM (see Figure 4.4). In this way, the output powers of each signal (Stokes and residual) can be separated for further analysis of its evolution under the gradual increase in coupled pump power; these are represented in Figure 4.5.

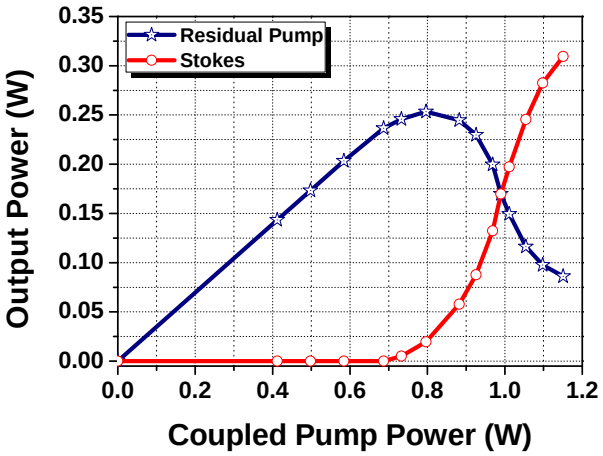

Figure 4.5: Power delivered by the Stokes as a function of coupled pump power

Table 4.1: Values of: threshold power (yellow), critical power (orange) and maximum Stokes power (gray) delivered as a function of coupled pump power (C.P.P.), corresponding to Figure 4.5

C.P.P [W]	Residual Pump [W]	Stokes [W]
0.690	0.237	6.408E-6
0.990	0.170	0.170
1.150	0.086	0.309

Note in Figure 4.5 that the evolution of the residual pump (blue line with stars) is linear for coupled pump powers < 0.69 W; i.e., its slope is constant within that range of powers since practically the Stokes signal is absent. This is the linear regime of the system that describes an elastic reaction of the molecules that compose the core of the fiber [80]. Within the linear regime, we quantify the losses of the fiber.

The mechanism is simple, knowing the coupled power and the power delivered at the output of the 4.8 km of fiber, we calculate the transmittance with equation (2.4), and using equation (2.5) we quantify the loss. Table 4.2 presents the average fiber losses obtained from six measurements made.

Table 4.2: Measurement of: coupled powers $P_{(input)}$, emitted powers $P_{(output)}$, transmittance (T), and fiber attenuation (α)

$P_{(input)}$[W]	$P_{(output)}$[W]	T	$\alpha[Km^{-1}]$
0.178	0.060	0.337	0.227
0.261	0.089	0.341	0.224
0.349	0.120	0.344	0.222
0.498	0.173	0.347	0.221
0.584	0.202	0.346	0.221
0.669	0.231	0.345	0.222
	Averages =	**0.343**	**0.223**

Now, using equation (2.13) with $\alpha = 0.223$, we calculate the effective length of the fiber, obtaining $L_{eff} \approx 2.95$ Km.

Returning to Figure 4.5, at ∼0.69 W, the system reaches the threshold; i.e., the boundary between linear and non-linear behavior. So, we say that 0.69 W is the threshold power (P_{th}). At coupled pump powers > 0.69 W, SRS predominates; therefore, the slope is no longer constant. This is a manifestation of gain or loss of energy (inelastic behavior of the molecules); i.e., between 0.69 W and 0.99 W, the slope of the residual signal decreases since the pump is transferring energy to the Stokes, producing an inverse result on the slope of the Stokes signal, observe the red-dashed line bending upwards. Note that at 0.99 W (critical power), the Stokes power equals the residual power; therefore, the energy transfer, at that point, is maximum because the slope of the Stokes curve reaches its greatest slope. On the other hand, for coupled powers > 0.99 W, the slope of the Stokes gradually decreases by: (a) giving energy back to the pump an anti-Stokes behavior and/or (b) starts to produce the second Stokes as described in [85]. These signals were not considered since the energy transfer was very weak, limited by the low pump powers used in the configuration whose WDM1 was a low power device.

Figure 4.6 shows the spectral behavior of the Stokes slightly above the threshold (0.73 W) and at the critical power (0.99 W). It is possible to observe in the inset of Figure 4.6a that multiple unstable peaks are competing to grow up (1116.2 nm, 1116.5 nm, 1116.7 nm, and 1117 nm); these appeared slightly beyond the threshold, with a bandwidth covering ∼2 nm (1115.7 nm - 1117.7 nm) and centered at 1116.5

nm (maximum intensity). Within this range of wavelengths, we highlight the Stokes component at 1116.15 nm, which later acquires great importance. On the other hand, Figure 4.6b, at 0.99 W coupled pump power, shows two strong bands, the 1117.1 nm and an additional band centered at 1122.4 nm. These bands correspond respectively to the frequency shift peaks at 13.1 THz and 14.5 THz of the Raman gain spectrum for silica molecules when pumped at 1064 nm (see Figure 1.5) [86].

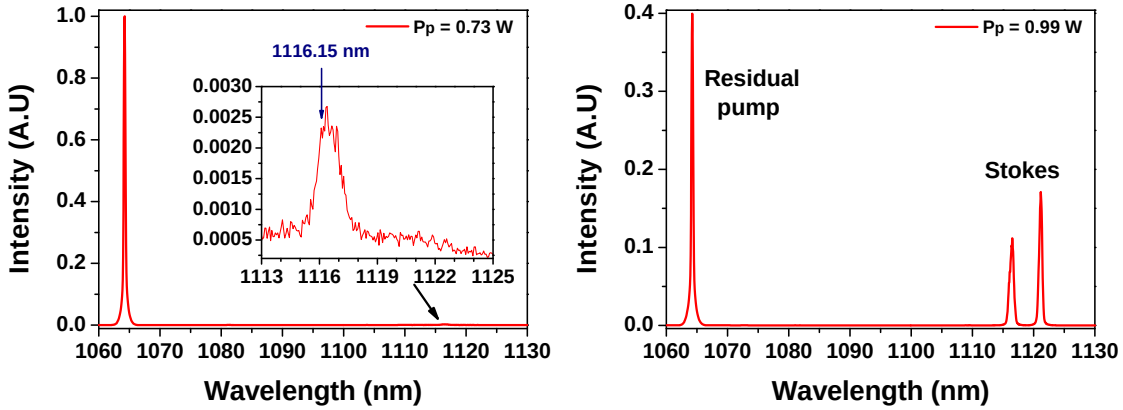

(a) (b)

Figure 4.6: a) Stokes response at 0.73 W coupled pump, and b) Stokes response at 0.99 W coupled pump

We also measured, at the output of arm 2, the backward-produced stokes signal (see Figure 4.1), which represents approximately 27.7% of the forward-produced Stokes power. To calculate how much backward-produced Stokes power the fiber delivered at point "b", we characterize the WDM1 with the amplified spontaneous emission of a pumped ytterbium-doped fiber, spliced directly in arm 3. This characterization allowed us to quantify the transmittance, through arms 1 and 2, as a function of the wavelength and the insertion loss of the device. The spectral response of transmittance is shown in Figure 4.7.

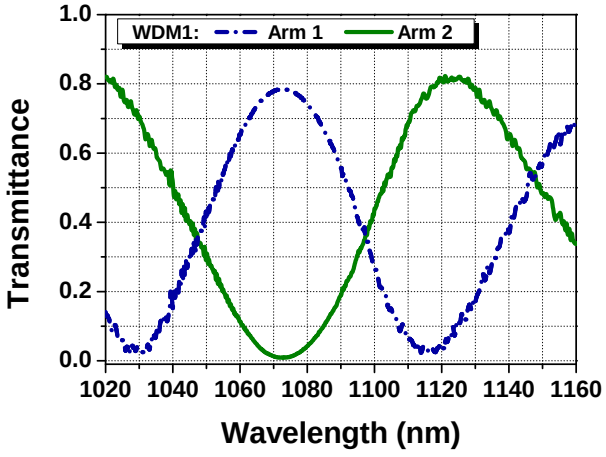

Figure 4.7: Transmittance of WDM1 (signals applied to arm 3) as a function of wavelength.

Note that at 1116 nm the transmittance in arm 2 is around 77%, and in arm 1 it is around 3%; therefore, the loss at 1116 nm is approximately 20%. Now, if the sum of Stokes signals delivered by arms 1 and 2 are compensated with the loss of the device, at point "b" the backward-produced Stokes signal is approximately 36% of the forward-produced Stokes power.

Up to this point, except for the type of WDM1 used, nothing is new; the system behaves as expected in a free-running configuration. Our contribution consists of a notable improvement when the initial scheme was modified to a ring cavity with insertion of a Fabry-Perot filter, and when three meters of ytterbium-doped fiber were spliced to the laser cavity. Before implementation of the ring cavity configuration, we started by splicing a WDM in the output end of the RGF as shown in Figure 4.8.

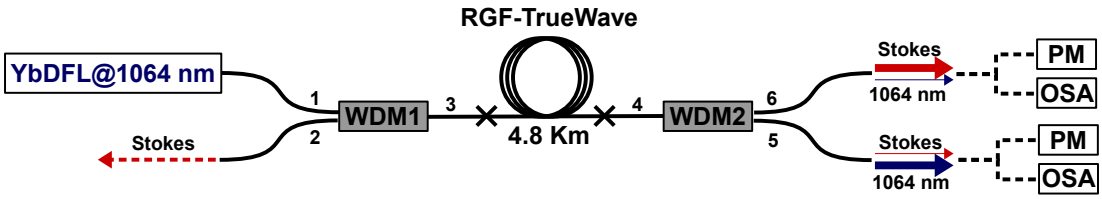

Figure 4.8: Experimental setup of the free-running Raman laser.

The RGF output was coupled to arm 4 of the second WDM2 that was very lossy, delivering through arms 5 and 6 together approximately 45% of the coupled input power (∼55% insertion loss). From this power, the WDM2 delivers 85% of the Stokes component (∼1116 nm) and 15% of the residual pump (1064 nm) out of arm 6; whereas the opposite, 15% of Stokes and 85% of pump, occurs out of arm 5. This is supported by characterizing the transmittance spectrum of WDM2 as shown in Figure 4.9.

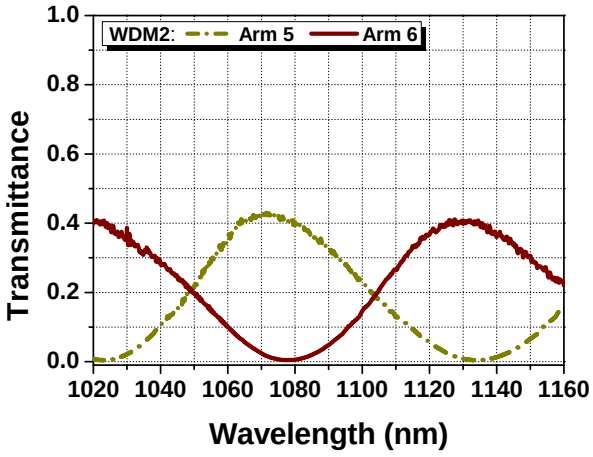

Figure 4.9: Transmittance of WDM2 as a function of wavelength.

Let us present in Figure 4.10 the evolution of the mixture of emitted signals by arm 5.

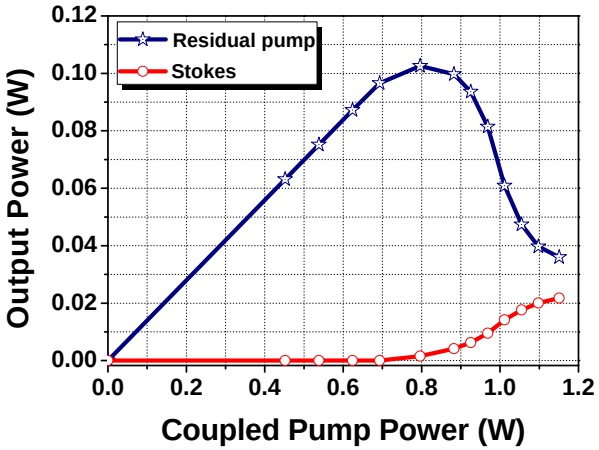

Figure 4.10: Power delivered by the Stokes as a function of pump power

In Figure 4.5 we saw that the power delivered by the residual and Stokes signals were equal for a coupled power of 0.99 W. In contrast, Figure 4.10 shows that this behavior does not take place; because, as we already mentioned, only 15% of the Stokes signal is transmitted by arm 5. This small Stokes component (red-dashed line) becomes the seed that urges the process of amplification, once the ring cavity is closed, and reduces the oscillation threshold as we will see later.

The response of the Stokes to different pump powers is presented in Figure 4.11a; just above threshold, at 0.69 W. On the other hand, the emitted spectrum far above threshold, at 0.99 W pump power is shown in Figure 4.11b.

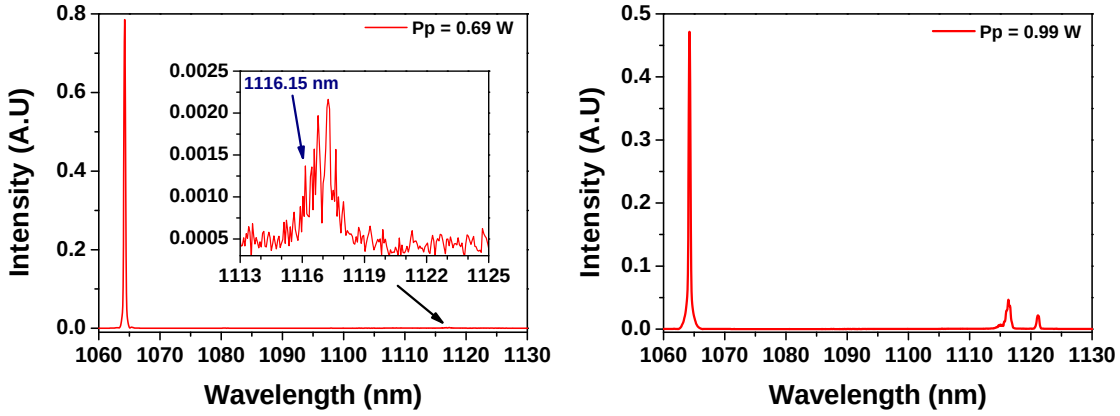

(a) (b)

Figure 4.11: a) Emitted spectrum at 0.69 W coupled pump, and b) Emitted spectrum at 0.99 W coupled pump

The inset in Figure 4.11a magnifies the part of the band that contains multiple competing laser lines within a spectral range of ∼4 nm (1115-1119 nm); each line is less than 1nm in width and they were quite unstable, the strongest one was situated at 1116.7 nm and 1117.2 nm. Within the multiple lines, we again highlight the component at 1116.15 nm that corresponds to the 13.2 THz Raman peak. On the

other hand, Figure 4.11b shows two competing Stokes signals at 1117.4 and 1122.3 nm (maximum intensity, 14.1 THz peak). These spectra are representative of the main mixed signals generated by the fiber and emitted through arm 5 of the WDM2.

Now, let us focus our attention on the evolution of the delivered and usable power of our system, extracted through arm 6 (Figure 4.8), where ∼85% of the delivered power corresponded to Stokes and ∼15% to the residual pump. The energy transfer evolution of the delivered signals (Stokes and residual) as a function of the coupled pump is shown in Figure 4.12.

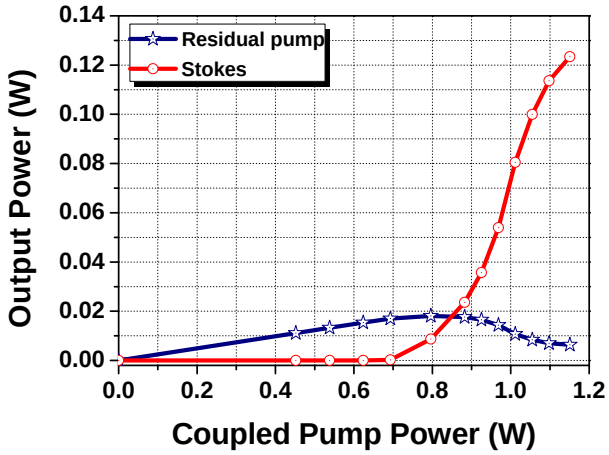

Figure 4.12: Output delivered powers of Stokes and residual pump as a function of coupled pump power

Table 4.3: Values of: threshold power (yellow), critical power (orange) and maximum Stokes power (gray) delivered as a function of coupled pump power (C.P.P.), corresponding to Figure 4.12

C.P.P [W]	Residual Pump [W]	Stokes [W]
0.690	0.017	2.705E-6
0.990	0.012	0.068
1.150	0.006	0.123

Unlike the evolution of the Stokes presented in Figure 4.10, note in Figure 4.12 that at coupled powers > 0.85 W, the Stokes exceeds the power levels delivered by the residual signal. This behavior of the Stokes is taken as a reference to compare the response of the Stokes under conditions of improvements sequentially implemented to the configuration as it will be presented in the following sections.

On the other hand, the response of the Stokes to different pump powers is presented in Figure 4.13. It is possible to observe in the inset of Figure 4.13a that multiple unstable peaks are competing to grow up (1116 nm, 1116.4 nm, 1116.7 nm, 1117 nm,

1117.2 nm, and 1117.5 nm); these appeared just above threshold (0.69 W), within a bandwidth covering ∼2.5 nm (1115.8 nm - 1118.3 nm) and centered at 1117.2 nm (maximum intensity). Farther up from the threshold (at 0.99 W), Figure 4.13b shows two strong bands, the 1117.5 nm and an additional band centered at ∼1122.5 nm. The inset in Figure 4.13b shows more detail, note that each strong band has two small sub bands, 1116.9 nm and 1117.6 nm for the first band and, 1122.2 nm and 1122.5 nm for the second one. The selection of these bands can be controlled by temperature variations of the RGF as they correspond to the most resonant phonons of silica, the 13.2 and 14.1 THz ones.

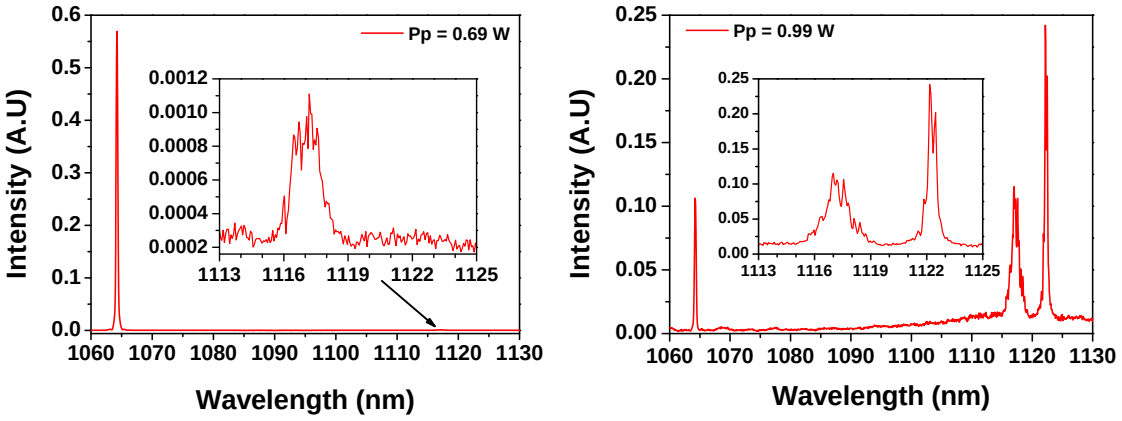

(a) (b)

Figure 4.13: a) Stokes response at 0.69 W coupled pump, and b) Stokes response at 0.99 W coupled pump

Next, a ring-cavity configuration was implemented; for this, arm 5 was spliced to arm 2 as shown in Figure 4.14.

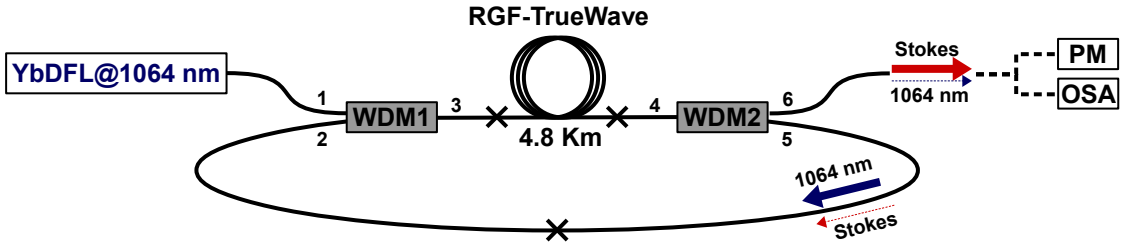

Figure 4.14: Modified experimental setup to a ring-cavity Raman fiber laser

With ring-cavity configuration, the small Stokes signals (corresponding to 15% delivered by arm 5) became the seed that re-feed the system. This sped up and reinforced the energy transfer to Stokes process by further demanding energy from the pump, improving in such a way the conversion efficiency. This is supported by Figure 4.15, where it is shown that the oscillation threshold occurred at ∼0.61 W instead of the ∼0.69 W of the previous one. This represents a reduction of ∼11.6% (∼80 mW from the pump) compared to the threshold in the previous setup (Fig.

4.12). Now, note that at maximum coupled-pump power (1.15 W), the delivered power by the Stokes was 150 mW compared to 123 mW of the previous one, this represents an increase of ∼22% (∼27 mW). Furthermore, the slopes of the Stokes evolution in Figure 4.15 are steeper than those obtained previously, which indicates an improvement in the energy transfer between signals, mostly in the 0.75 W - 0.9 W interval.

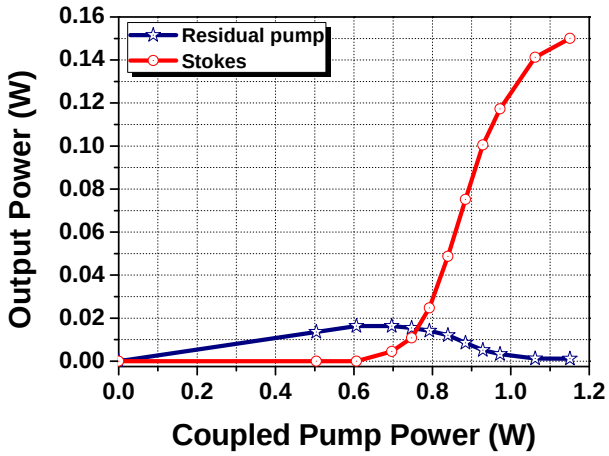

Figure 4.15: Power delivered by the Stokes as a function of pump power

Table 4.4: Values of: threshold power (yellow), critical power (orange) and maximum Stokes power (gray) delivered as a function of coupled pump power (C.P.P.), corresponding to Figure 4.15

C.P.P [W]	Residual Pump [W]	Stokes [W]
0.610	0.016	0.705E-6
0.990	0.003	0.123
1.150	0.001	0.150

Regarding the spectral composition of the Stokes signal, Figure 4.16a shows the output spectrum in Arm 6, just above the threshold (0.63 W pump). The inset magnifies the band that contains four competing signals with a bandwidth of ∼1.4 nm (1114.9 nm - 1116.3 nm). Interestingly, only the shorter-wavelength portion of the main band, which was present in the former arrangement, becomes amplified with peaks centered at 1115.1 nm, 1115.5 nm, 1115.8 nm, and 1116.2 nm; each peak is less than 0.5 nm wide. As there is a reduction of the amplified band, the signals are quite stronger compared to the simple RFL. This interesting effect suggests that these types of lasers in ring configurations have a preference for amplifying the first generated wavelength components. This effect seems very consistent even at higher pump powers. See Fig.4.16b. Further increasing from the threshold, at 0.88 W pump, only the shorter wavelength band below 1120 nm from the previous arrangement becomes amplified composing a single wide-band of ∼5 nm (1115 nm - 1120 nm); even

more, observe that the shorter wavelengths within the band itself are more favored for amplification.

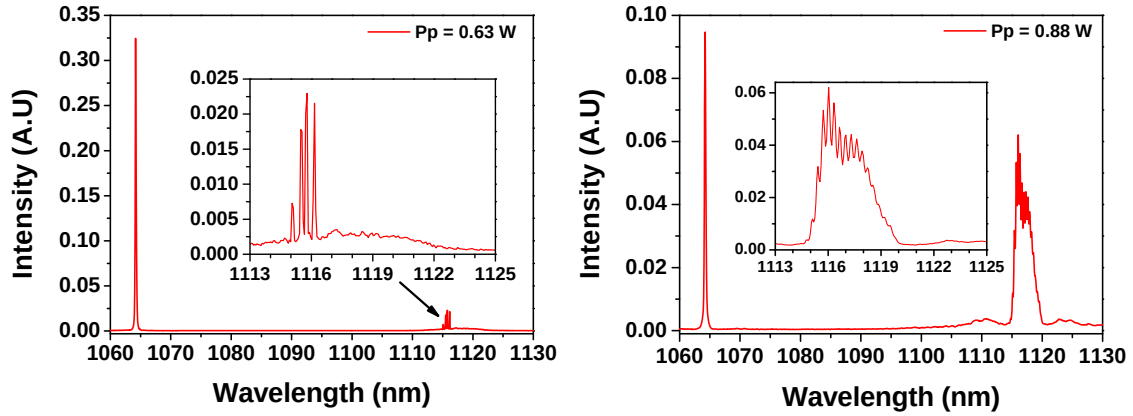

(a) (b)

Figure 4.16: a) Stokes response at 0.63 W coupled pump, and b) Stokes response at 0.88 W coupled pump

The fact that the second main band does not oscillate reinforces such annotation. This blue-shifted behavior makes sense since a more efficient system operates at lower temperature and hence the less energy vibrating bands of silica molecules centered at 13.2 Thz dominate. Therefore, in our system, the first wavelength components that oscillate, and re-circulate, strongly define the feedback within the cavity, inhibiting in this way the others to compete; in this way, the medium tends to be locked to oscillate at the shorter wavelengths. Thus, the three strongest peaks are centered at 1115.8 nm, 1116 nm, and 1116.2 nm respectively. From here, laser emission can be tuned to any wavelength that covers this emission band as described at the next stage.

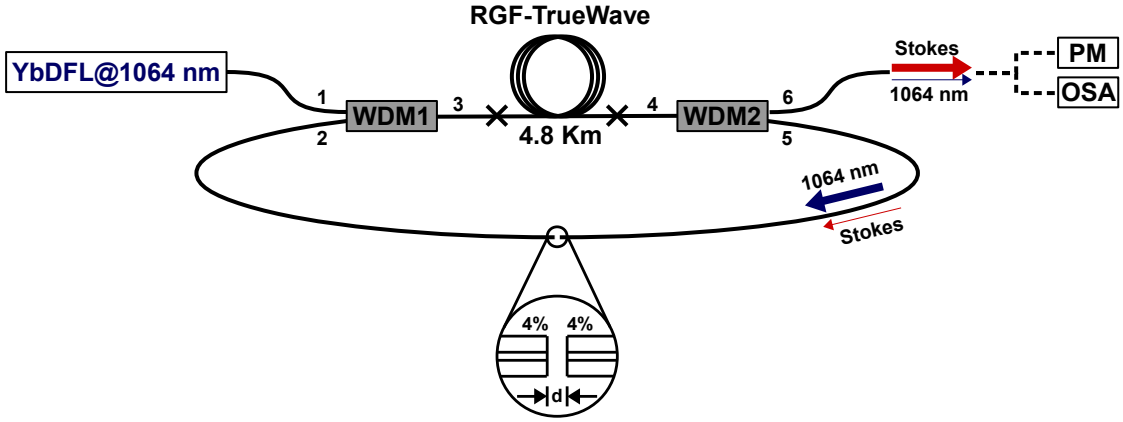

Figure 4.17: Experimental diagram of the Raman ring-cavity plus the insertion of a Fabry-Perot interferometer (FPI)

In order to pick a single-line laser to oscillate, FP intra-cavity was introduced. In order to do this, the arms 2 and 5, perpendicularly-cleaved, were aligned very close to each other (d-spacing of some microns) as shown in the zoomed image in Figure

4.17. Under this configuration, the fibers had to be perfectly aligned and their ends completely flat to operate as FPI. By varying the d-parameter, certain line(s) selection was achieved as in [87] and [88]; then one or more axial-modes were selected for oscillating as in reference [78]. One important characteristic of this device is that polarized light is no required.

Tests were performed with several d-separations. Logically, large d-separations implied poor feedback. In contrast, short d-separations allowed good feedback and single-axial mode filtering. This can be seen in Figure 4.18, where the transmittance at different d-separations and the mode filtering are shown when passing white light through the FP optical fiber alone.

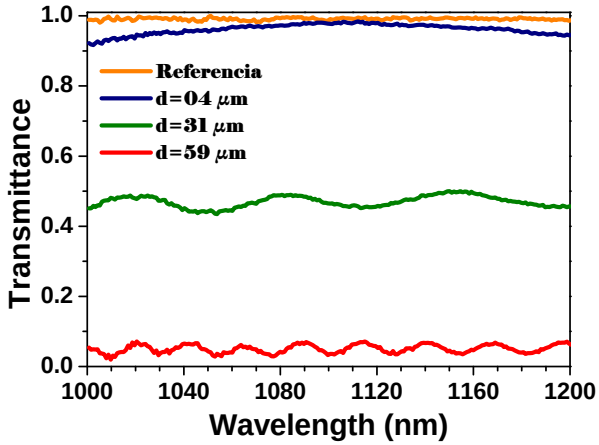

Figure 4.18: Filtering of the Fabry-Perot interferometer with different d-separations.

Observe for example that for $d \approx 4\mu m$, the FPI attained a single fringe, improving in this way, the conversion efficiency and line selectivity compared to the former a management with maximum transmittance around the first Stokes signal. Figure 4.19 shows the Stokes evolution curve as a function of the coupled pump power.

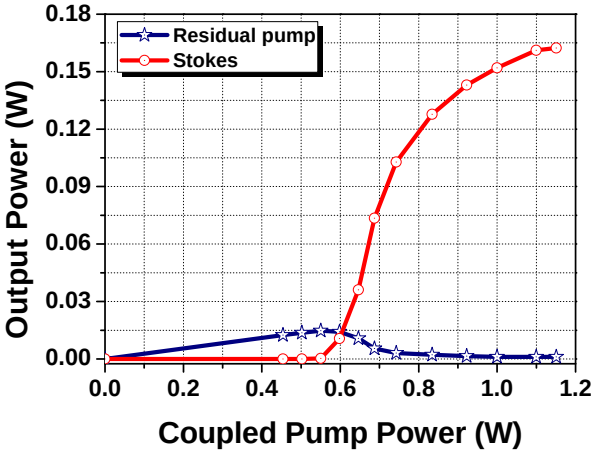

Figure 4.19: Power delivered by the Stokes as a function of pump power

Table 4.5: Values of: threshold power (yellow), critical power (orange) and maximum Stokes power (gray) delivered as a function of coupled pump power (C.P.P.), corresponding to Figure 4.19

C.P.P [W]	Residual Pump [W]	Stokes [W]
0.550	0.014	3.105E-6
0.990	0.001	0.150
1.150	0.001	0.162

Please note that the effect of filtering, by the FPI, reduced further the laser oscillation threshold down to 0.55 W (∼10%, 60 mW), compared to the system without FPI. Considering the gain region (0.55 W - 0.7 W) in Figure 4.19, the slope of the Stokes curve (red-dashed line) is even steeper than in the former setups. In addition, at maximum coupled power (1.15 W), the Stokes delivered ∼8% more power than in the scheme without FPI (Fig.4.15). It is clear that there is a performance improvement in the energy transfer mechanisms from pump to Stokes signals.

Apart from enhancing the energy transfer, this FPI filtering scheme concentrates the energy that was spread among several modes in the former schemes, into a single line centered at ∼1116.15 nm with ∼0.18 nm FWHM linewidth above the threshold. Please, see the well-defined, and stable low-intensity line presented in the inset in Figure 4.20a.

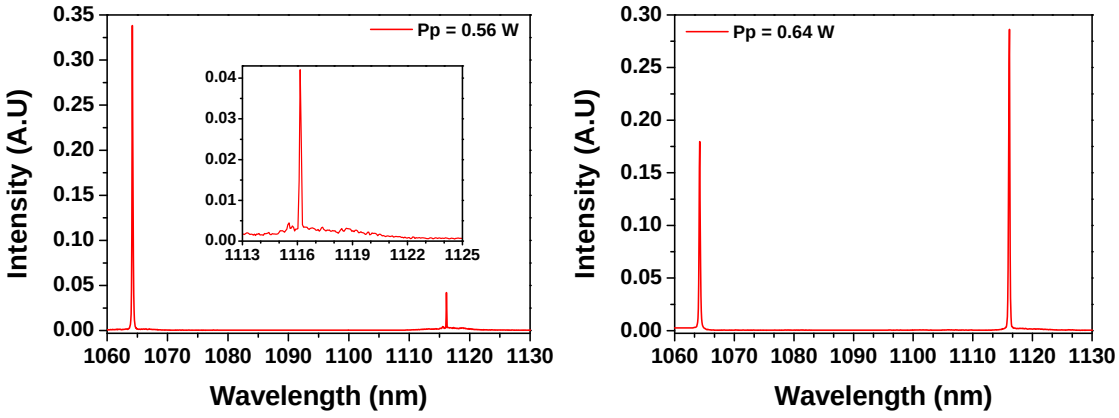

(a) (b)

Figure 4.20: a) Stokes response at 0.56 W coupled pump, and b) Stokes response at 0.64 W coupled pump

Farther away from the threshold, Figure 4.20b shows the output spectrum at 0.64 W coupled pump power. Note that the same well-defined and highly stable laser line was preserved and hence this signal contained all the Stokes energy. This behavior allows us to infer that the FPI forced the system to oscillate within the modal band of the interferometer, rejecting parasitic modes, and reinforcing a single mode that

oscillates easily. Now observe that the linewidth of the Stokes signal is around 0.4 nm, very similar to the pump laser. These results make us affirm that under this configuration the improvements are quite significant, a defined and stable oscillation with a relatively low threshold has a positive impact on the conversion efficiency. This is extremely useful for cascade laser applications, where higher-order Stokes components are required.

In addition to the later setup, another improvement was implemented that increased, even more, the conversion efficiency and decrease the oscillation threshold. Our new experimental arrangement consisted on splicing 3-m of YbDF (Thorlabs YB1200-6/125DC) within the Raman cavity; except for the dopants contained, the fiber was practically identical to the RGF. The new modified arrangement is described in Figure 4.21.

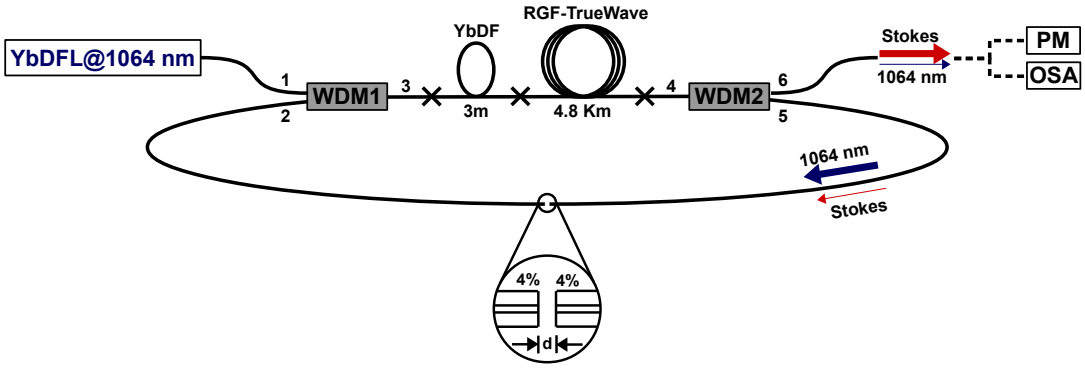

Figure 4.21: Experimental diagram of the Raman ring-cavity plus the insertion of a Fabry-Perot interferometer and 3 meters of Yb^{3+}-doped fiber

At this point, we invite you to see Figure 4.22. Please note in Figure 4.22 that the YbDF weakly absorbs the 1064-nm pump, approximately 20 dB/km; therefore, we can say that the YbDF is practically transparent at that wavelength, but due to the high-power density passing through, it is sufficient to produce an ASE signal up to (close to) 1200 nm [79, 80].

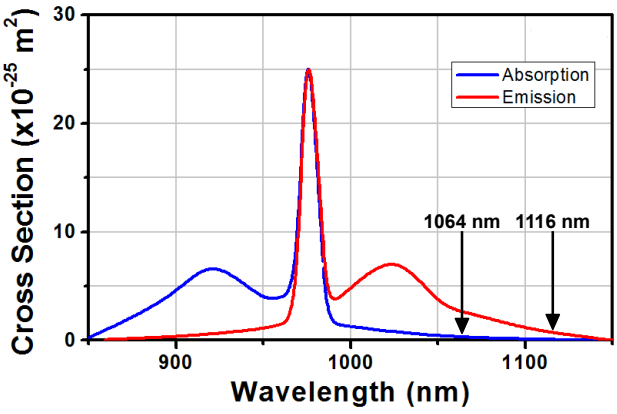

Figure 4.22: Ytterbium-doped fiber absorption and emission cross sections

Some of the ASE signals coincide with the Stokes signal (1116 nm) and collaborate to have a stronger "trigger" signal that will be available to assist the SRS starts as soon as it takes place [79, 80]. As an effect, a significant reduction in the oscillation threshold and improvements in the conversion efficiency are observed. The main results of this configuration are presented in Figure 4.23.

Note from Fig.4.23a that a further improvement in the laser performance was present; the oscillation threshold decreased to 0.5 W, which corresponds to an additional ∼9.1% improvement. Likewise, the slope in the evolution curve is even steeper compared with any of the previous experiments. Also note from Fig.4.23b a single sharp line centered at 1116.15 nm with great stability and a ratio Stokes-to-pump (peak-stokes intensity/peak-pump intensity) close to 6.

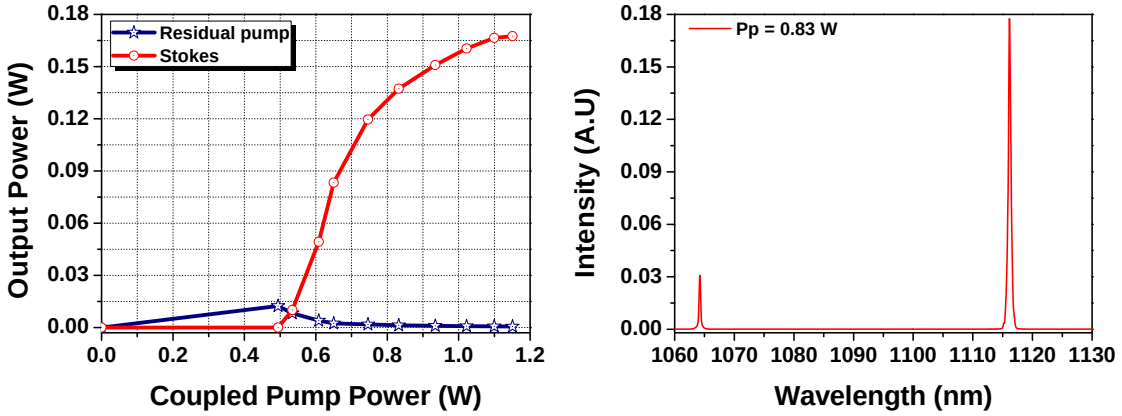

(a) (b)

Figure 4.23: a) Power delivered by the Stokes as a function of pump power, and b) Stokes response to 0.83 W coupled pump

Table 4.6: Values of: threshold power (yellow), critical power (orange) and maximum Stokes power (gray) delivered as a function of coupled pump power (C.P.P.), corresponding to Figure 4.23a

C.P.P [W]	Residual Pump [W]	Stokes [W]
0.5	0.014	1.405E-6
0.990	0.001	0.155
1.150	0.001	0.168

The results obtained allow us to affirm that hybrid-cavities (doped fibers in Raman laser cavities) mainly enhance the conversion efficiency. It is worth noting that our experimental setup still has a niche of opportunities to improve its efficiency; for example, WDMs present significant losses, the doped-fiber length should be optimized, it is also possible to improve the ASE level by applying heat to the YbDF that causes a fluorescence shifting to longer wavelengths as in [89]. Also, the RGF was longer

than required because the WDM1 was recommended to handle no more than approximately 1.5 Watt; in this way, we assured the characterizations of the arrangements within such a low-power range.

To summarize and easily compare the results regarding pump thresholds and efficiencies of the different configurations along all the experiments realized here, we composed Figure 4.24, where we present all the efficiency-related curves.

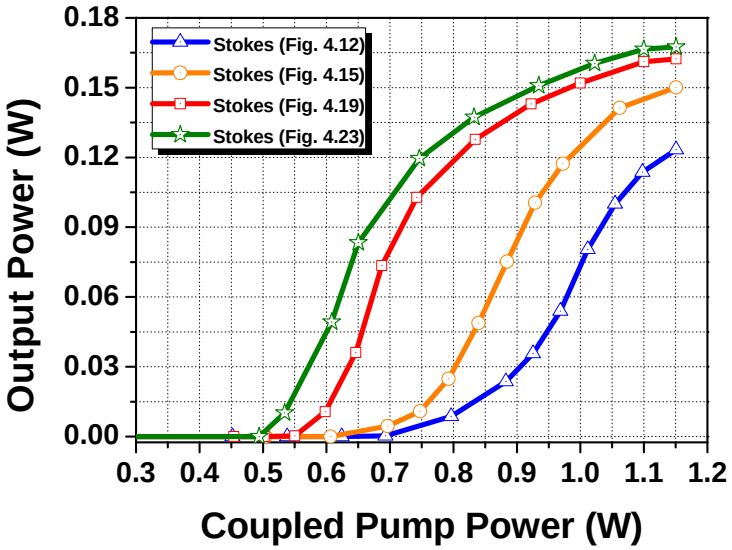

Figure 4.24: Evolution of the Stokes signal throughout all the experimental stages.

From these results, we may affirm that for the changes that were sequentially introduced, each one of them implied an improvement on both parameters, the decrease of pump threshold and the increase of efficiency. Note the clear improvements of the operating threshold that decreased from 0.69 W to 0.5 W that corresponds to a ∼28% overall reduction; regarding efficiency, the increase of the slope of the curves together with increments on the delivered power for the maximum pump applied took place, from around 123 mW to 168 mW, clearly represents a 36.6%-improvement.

4.4 Conclusions

We have proposed here a series of improvements that might be considered as alternatives to enhance the performance of Raman fiber lasers. Such improvements produce several benefits such as a general efficiency increase with a lower threshold, compared to a simple Raman fiber laser configuration, together with filtering for single-line emission instead of multi-line and/or multi-band emission that tends to produce instabilities caused by mode competition. A single-line (around 0.4 nm wide) and very stable Stokes at 1116.15 nm was achieved with the most complete configuration, this is extremely useful for cascade lasers, where higher-order Stokes components are required. The optimizations of some parameters of this non-optimized system open

possibilities to take it as a base for high-power hybrid fiber lasers. We consider this a small contribution to enhancing the performance and efficiency of these types of fiber lasers.

In the future, we will develop a model of the hybrid fiber laser to optimize the various parameters present in the proposed scheme; thus, identify the optimal Raman fiber and ytterbium fiber length, calculate more accurately the coupling ratio (in WDMs) for each wavelength, determine the best location of the FP-filter inside the cavity, etc. All this to improve energy conversion efficiency, further reducing threshold power and critical power.

Bibliography

[1] G. P. Agrawal. "Fiber-Optic communication systems". *In Fiber-Optic communication systems*, 4th Edition:pp.1–600, 2011.

[2] Heodore H. Maiman. "Stimulated optical radiation in ruby". *Nature*, Vol.187:pp.493–494, 1960.

[3] S. Babin, C. Dmitriy, K. Sergey, R. Michail, and V. Alexander. "All-fiber widely tunable Raman fiber laser with controlled output spectrum". *Optics Express*, Vol.15, no.13:pp.8438–8443, 2007, doi:10.1364/OE.15.008438.

[4] N. Bloembergen. "The Stimulated Raman Effect". *American Journal of Physics*, Vol.35, no.11:pp.989–1023, Nov.1967, doi:10.1119/1.1973774.

[5] G. Agrawal. "Nonlinear fiber optics: its history and recent progress [invited]". *Journal of the Optical Society of America B*, Vol.28, no.12:pp.A1–A10, Dic.2011, doi:10.1364/JOSAB.28.0000A1.

[6] R. Smith. "Optical power handling capacity of low loss optical fibers as determined by stimulated Raman and Brillouin scattering". *Applied Optics*, Vol.11, no.11:pp.2489–2494, Nov.1972, doi:10.1364/AO.11.002489.

[7] L. de la Cruz-May, J. Álvarez-Chávez, E. Mejía, A. Flores-Gil, F. Méndez, and S. Wabnitz. "Raman threshold for nth-order cascade Raman amplification". *Optical Fiber Technology*, Vol.17, no.3:pp.214–217, May.2011, doi:10.1016/j.yofte.2011.02.002.

[8] M. N. Islam. "Raman amplifiers for telecommunications: Physical principles". *Springer*, New York:Chapter 1, 2004.

[9] Barry R. Masters. "C. V. Raman and the Raman effect". *OPN*, pages pp.40–45, March 2009.

[10] C. Huang, Z. Cai, C. Ye, H. Xu, and Z. Luo. "Analytic modeling of the p-doped cascaded Raman fiber lasers". *Opt. Fiber Technol*, Vol.13, Issue 1:pp. 22–26, Jan.2007, doi:10.1016/j.yofte.2006.03.002.

[11] M. Farahani and T. Gogolla. "Spontaneous Raman scattering in optical fiber with modulated probe light for distributed temperature Raman remote sensing". *Journal of lightwave Technology*, Vol.17, Issue 8:pp.1379–1391, Aug.1999, doi:10.1109/50.779159.

[12] N. Colthup, L. Daly, and S. Wiberly. "Introduction to infrared and Raman spectroscopy". *Third edition, Academic Press*, 1990.

[13] K. O. Hill, B. S. Kawasaki, and D. C. Johnson. "Low-threshold cw Raman laser". *Applied Physics Letters*, Vol.29, no.3:pp.181–183, Aug.1976, doi:10.1063/1.89016.

[14] A. Smekal. "Zur quantentheorie der dispersion". *Naturwissenschaften*, Vol.11. Issue 43:pp.873–875, Oct.1923, doi:10.1007/BF01576902.

[15] C. V. Raman and N. N. Nathe. "The diffraction of light by high frequency sound waves: Part I". *Proc. Indian Acad. Sci.-Sect.A*, Vol.2, Issue 4:pp.406–412, Oct.1935, doi:10.1007/BF03035840.

[16] G. Eckhardt, R. W. Hellwarth, F. J. McClung, S. E. Schwarz, D. Weiner, and E. J. Woodbury. "Stimulated Raman Scattering From Organic Liquids". *Phys. Rev. Lett.*, Vol.9, Issue 11:pp.455–457, Dic.1962, doi:10.1103/PhysRevLett.9.455.

[17] R. Loudon. "Theory of stimulated Raman scattering from lattice vibrations". *Proc. Phys. Soc*, Vol.82, Issue 3:pp.393–400, May.1963, doi:10.1088/0370-1328/82/3/309.

[18] Y. R. Shen and N. Bloembergen. "Theory of stimulated Brillouin and Raman scattering". *Phys. Rev.*, Vol.137, Issue 6A:pp.1787–1805, March 1965, doi:10.1103/PhysRev.137.A1787.

[19] S. P. Singh, R. Gangwar, and N. Singh. "Nonlinear scattering effects in optical fibers". *Progress in Electromagnetics Research*, Vol.74:pp.379–405, 2007, doi:10.2528/PIER07051102.

[20] F. Forghieri, R. W. Tkach, and A. R. Chraplyvy. "Fiber nonlinerities and their impact on transmission systems". *Optical Fiber Telecommunications-III, I. P. Kaminow and T. L. Koch (eds)*, Vol.A:Academic Press, New York, 1997.

[21] R. W. Hellwarth. "Theory of stimulated raman scattering". *Phys. Rev.*, Vol.130, Issue 5:pp.1850–1852, June 1963, doi:10.1103/PhysRev.130.1850.

[22] K.-H. Chen and Kuei-Hsien. "Spontaneous Raman and coherent anti-stokes Raman spectroscopy of infrared multiphoton-excited molecules.". *Thesis (Ph.D)-Harvard Univ. Source Diss. Abstr. Int.*, Vol.50-12, Sec.B:pp.5696, (1989).

[23] S. Lewis, V. Chernikov, and R. Taylor. "Temperature dependent gain and noise in fiber raman amplifier". *Opt. Lett*, Vol.24, no.24:p.1823–1825, Dec.1999, doi:10.1364/OL.24.001823.

[24] R. W. Boyd. "Nonlinear Optics, Third Edition". *In Fiber-Optic communication systems*, pages 473–508, Oct.2007.

[25] G. P. Agrawal. "Nonlinear fiber optics". *4th edition, Elsevier Academic Press, San Diego*, 2007.

[26] C. Wang. "Theory of Stimulated Raman Scattering". *Phy. Review*, Vol.182, Issue 2:pp.482–494, Jun.1969, doi:10.1103/PhysRev.182.482.

[27] J. Bromage. "Raman Amplification for fiber Communications Systems". *J. Light. Technol.*, vol.22, no.1:pp.79–93, Jan.2004, doi:10.1109/JLT.2003.822828.

[28] C. O. Frazao, G. M.T.M. Rocco, M.B. Marques, H.M. Salgado, M.A.G. Martinez, J.C.W.A. Costa, A.P. Barbero, and J.M. Baptista. "Stimulated Raman Scattering and its Applications in Optical Communications and Optical Sensors". *The Open Optics Journal*, vol.3, no.1:pp.1–11, Feb.2009, doi:10.2174/1874328500903010001.

[29] Q. Lin and G. Agrawal. "Statistics of polarization-dependent gain in fiber-based raman amplifiers". *Optics Letters*, vol.28, Issue.4:pp. 227–229, Feb.2003, doi:10.1364/OL.28.000227.

[30] R. Stolen. "Polarization effects in fiber raman and brillouin lasers". *IEEE Journal of Quantum Electronics*, vol.15, Issue.10:pp.1157–1160, Oct.1979, doi:10.1109/JQE.1979.1069913.

[31] G. P. Agrawal. "Fiber-Optic communication systems". *3th Edition. Wiley Interscience*, Chapter 6:pp.243–244, 2002.

[32] C. Lin, L.G. Cohen, R.H. Stolen, G.W. Tasken, and W.G. French. "Near-infrared sources in the 1-1.3 μm region by efficient stimulated Raman emission in glass fibers". *Optics Communications*, Vol.20, Issue.3:pp.426–428, Mar.1977, doi:10.1016/0030-4018(77)90221-8.

[33] Y. Murakami, K. Noguchi, F. Ashiya, Y. Negishi, and N. Kojima. "Maximum Measurable Distances for a Single-Mode Optical Fiber Fault Locator Using the Stimulated Raman Scattering (SRS) Effect". *IEEE Transactions on Microwave Theory and Techniques*, Vol.30, Issue.10:pp.1461–1465, Oct.1982, doi:10.1109/TMTT.1982.1131278.

[34] J. AuYeung and A. Yariv. "Theory of CW Raman oscillation in optical fibers". *Journal of the Optical Society of America*, vol.69, Issue.6:pp.803–807, Jun.1979, doi:10.1364/JOSA.69.000803.

[35] J. A. Buck. "Fundamentals of optical fibers". *New York: Wiley-Interscience*, 2004.

[36] L. de la Cruz-May, E. B. Mejía, O. Benavides, J. V. Jiménez, J. C.Chacón, and M. May-Alarcón. "Novel Technique for Obtaining the Raman Gain Efficiency of Silica Fibers". *IEEE Photonics Journal*, vol.5, no.4:pp.6100305, Aug.2013, doi:10.1109/JPHOT.2013.2271900.

[37] R. Paschotta, J. Nilsson, A. C. Tropper, and D. C. Hanna. "Ytterbium-doped fiber amplifiers". *IEEE J. Quantum Electron*, vol.33, no.7:pp.1049–1056, Jul.1997, doi:10.1109/3.594865.

[38] I. Mandelbaum and M. Bolshtyansky. "Raman amplifier model in single-mode optical fiber". *IEEE Photonics Technology Letters*, vol.15, no.12:pp.1704–1706, Dec.2003, doi:10.1109/LPT.2003.819760.

[39] M. N. Islam. "Raman amplifiers for telecommunications". *IEEE Journal of Selected Topics in Quantum Electronics*, vol.8, no.3:pp.548–559, May.2002, doi:10.1109/JSTQE.2002.1016358.

[40] Y. Aoki. "Properties of fiber Raman amplifiers and their applicability to digital optical communication systems". *Journal of Lightwave Technology*, vol.6, no.7:pp.1225–1239, Jul.1988, doi:10.1109/50.4120.

[41] V. Supradeepa, Y. Feng, and J. Nicholson. "Raman fiber lasers". *Journal of Optics*, Vol.19, no.2:pp.023001, Jan.2017, doi:10.1088/2040-8986/19/2/023001.

[42] R. H. Stolen, E. P. Ippen, and A. R. Tynes. "Raman Oscillation in Glass Optical Waveguide". *Applied Physics Letters*, Vol.20, no.2:pp.62–64, Jan.1972, doi:10.1063/1.1654046.

[43] R. H. Stolen and E. P. Ippen. "Raman gain in glass optical waveguides". *Applied Physics Letters*, Vol.22, no.6:pp.276–278, March 1973, doi:10.1063/1.1654637.

[44] D. Mahgerefteh, B. Rosenberg, G. Burdge, D. Butler, and J. Goldhar. "Technique for measurement of the raman gain coefficient in optical fibers". *Optics Letters*, vol.21, no.24:pp.2026–2028, Dec.1996, doi:10.1364/OL.21.002026.

[45] K. Toge, K. Hogari, and T. Horiguchi. "Measurement of Raman gain distribution in optical fibers". *IEEE Photonics Technology Letters*, vol.14, no.7:pp.974–976, Jul.2002, doi:10.1109/LPT.2002.1012403.

[46] Y. Tsutsumi and M. Ohashi. "Simple technique for measuring Raman gain efficiency spectrum distribution in single-mode fiber". *in Proc. Asia Commun. Photon. Conf. Exhib., Opt. Soc. Amer.*, pages pp.1–6, Nov.2009, doi:10.1117/12.853074.

[47] J. Subías, J. Pelayo, C. Heras, P. Blasco, and R. Alonso. "Measurement of the effective area of non-linear power transfer in single-mode fibers due to stimulated Raman scattering". *Optics Communications*, vol.176, no.4-6:pp.387–392, Apr.2000, doi:10.1016/S0030-4018(00)00530-7.

[48] K. Rottwitt, J. Bromage, A. Stentz, L. Leng, M. Lines, and H. Smith. "Scaling of the raman gain coefficient: Applications to germanosilicate fibers". *Journal of Lightwave Technology*, vol.21, no.7:pp.1652–1662, Jul.2003, doi:10.1109/JLT.2003.814386.

[49] S. I. Kablukov, E. I. Dontsova, E. A. Zlobina, I. N. Nemov, A. A. Vlasov, and S. A. Babin. "An LD-pumped Raman fiber laser operating below 1 μm". *Laser Phys. Lett*, vol.10, no.8:p.085103, Aug.2013, doi:10.1088/1612-2011/10/8/085103.

[50] J. Zhou, J. Chen, X. Li, G. Wu, and Y. Wang. "Exact analytical solution for Raman fiber laser". *IEEE Photonics Technology Letters*, vol.18, no.9:pp.1097–1099, May.2006, doi:10.1109/LPT.2006.873961.

[51] Y. Zhao and S. D. Jackson. "Highly efficient free running cascaded Raman fiber laser that uses broadband pumping". *Opt. Express*, vol.13, no.12:p.4731, Jun.2005, doi:10.1364/OPEX.13.004731.

[52] I. Bufetov, M. Bubnov, V. Neustruev, V. Mashinsky, A. Shubin, M. Grekov, A. Guryanov, V. Khopin, E. Dianov, , and A. Prokhorov. "Raman Gain Properties of Optical Fibers with a High Ge-Doped Silica Core and Standard Optical Fibers". *Laser Physics*, vol.11, no.1:pp.130–133, Jan.2001.

[53] X. Shiqing, Y. Zhongmin, D. Shixun, Y. Jianhu, H. Lili, and J. Zhonghong. "Spectral properties and thermal stability of er^{3+}-doped oxyfluoride silicate glasses for broadband optical amplifier". *Journal of Alloys and Compounds*, vol.361, no.1-2:pp.313–319, Oct.2003, doi:10.1016/S0925-8388(03)00447-X.

[54] X. Wei, H. Yuwei, Z. Longjiang, Z. Zhiguo, and C. Wenwu. "Improved green upconversion emissions from $cawo_4 : Er^{3+} - yb^{3+}$ by cr^{3+} codoping for optical thermometry". *Journal of Luminescence*, vol.215:pp.116617, Nov.2019, doi:10.1016/j.jlumin.2019.116617.

[55] P. Yadav, C. Joshi, and S. Moharil. "Two phosphor converted white LED with improved CRI". *Journal of Luminescence*, vol.136:pp.1–4, Abr.2013, doi:10.1016/j.jlumin.2012.10.039.

[56] M. Digonnet. "Status of broadbandcrare-earth doped fiber sources for FOG applications". *Proc. SPIE Fiber Optic and Laser Sensors XI*, vol.2070:pp.113–131, Mar.1994, doi:10.1117/12.169896.

[57] W. J. Miniscalco. "Optical and Electronic Properties of Rare Earth Ions in Glasses, in Rare-Earth-Doped Fiber Lasers and Amplifiers". *In: Rare-Earth-Doped Fiber Lasers and Amplifiers*, Michael J.F. Digonnet:Ed.17–105, Marcel Dekker, BN 0-8247-0458-4, New York, (USA) 2001.

[58] G. Charalampides, K. Vatalis, B. Apostoplos, and B. Ploutarch-Nikolas. "Rare Earth Elements: Industrial Applications and Economic Dependency of Europe". *Procedia Economics and Finance*, vol.24:pp.126–135, 2015, doi:10.1016/S2212-5671(15)00630-9.

[59] M. J. Digonnet. "Continuos-Wave Silica Fiber Lasers, in Rare-Earth-Doped-Fiber Lasers and Amplifiers". *Marcel Dekker: New York*, Editor. 2001.

[60] J. Swiderski, A. Zajac, M. Skorcazkowiski, Z. Jankiewics, and P. Konieczny. "Rare-earth-doped high-power fiber lasers generating in near infrared range". *Opto-Electronics Review*, vol.12, no.2:pp.169–173, 2004.

[61] L. Pauling. "General Chemistry". *Ed. Dover*, 1st edition, NY, USA. 1988.

[62] S. Gasiorowicz. "Quantum Physics". *J.W, Wiley International Edition*, Third edition:Chapter 14, Apr.2003.

[63] Efraín Mejía-Beltrán. "Rare-Earth Doped Optical Fibers". *in Y. Moh, W. H. Sulaiman and A. Hamzah (Eds.), Selected Topics on Optical Fiber Technology*, Croatia; InTech, 2012.

[64] H. M. Pask, R. J. Carman, J. Robert, D. C. Hanna, A. C. Tropper, C. J. Mackechnie, and J. M. Dwes P. R. Barber. "Ytterbium-Doped Silica Fiber Lasers: Versatile Sources for the 1-1.2 μm Region". *IEEE J. Sel. Top. Quantum Electron*, Vol.1, no.1:pp.2–13, Apr.1995, doi:10.1109/2944.468377.

[65] W. H. Slabaugh and T. D. Parsons. "General Chemistry". First edition, NY 1966.

[66] H. Luu-Gen and S. Chen-Ke. "The Structural Investigation of a ZBLAN Glass by Vibrational Spectroscopy". *Chinese Journal of Physics*, Vol.34, No.5:pp.1270–1275, October 1996.

[67] L. Quin, Z. Shen, B. Low, H. Lee, T. Lu, D. Dai, S. Tang, and M. Kuok. "Crystallization Study of Heavy Metal Fluoride Glasses ZBLAN by Raman Spectroscopy". *Journal of Raman Spectroscopy*, Vol.28, No.5:pp.495–499, Jul.1997, doi:10.1002/(SICI)1097-4555(199707)28:7¡495::AID-JRS116¿3.0.CO;2-X.

[68] D. E. McCumber. "Einstein relations connecting broadband emission and absorption spectra". *Physical Review*, Vol.136, No.4A:pp.A954–A957, Nov.1964, doi:10.1103/PhysRev.136.A954.

[69] W. T. Carnall, P. R. Fields, and K. Rajnak. "Electronic energy levels in the trivalent lanthanide aquo ions". *J. Chem. Phys.*, Vol.49, No.10:pp. 4424–4442, Apr.1968, doi:10.1063/1.1669893.

[70] S. A. Lewis, S. Chernikov, and J. Taylor. "Fibre-optic tunable CW Raman laser operating around 1.3μm". *Opt. Commun.*, vol.182, no.4-6:pp.403–405, Aug.2000, doi:10.1016/S0030-4018(00)00790-2.

[71] S. Arun, V. Choudhury, R. Prakash, and V. R. Supradeepa. "High Power, Tunable, Continuous-wave Fiber Lasers in the L-Band Using Cascaded Raman Amplifiers". *IEEE Photonics Technol. Lett.*, vol.30, no.15:pp.1412–1415, Aug.2018, doi:10.1109/LPT.2018.2850850.

[72] Y. Li, J. Hou, J. Leng, W. Wang, and Z. Jiang. "Generation of Raman sidebands aided by a CW Stokes signal". *Opt. Laser Technol.*, vol.58:pp.215–219, Jun.2014, doi:10.1016/j.optlastec.2013.11.023.

[73] Y. Feng, L. R. Taylor, D. B. Calia, R. Holzlohner, and W. Hackenberg. "39W narrow linewidth raman fiber amplifier with frequency doubling to 26.5 w at 589 nm". *in Frontiers in Optics 2009/Laser Science XXV/Fall 2009 OSA Optics & Photonics Technical Digest*, page p.PDPA4, 2009, doi:10.1364/FIO.2009.PDPA4.

[74] D. Georgiev et al. "Watts-level frequency doubling of a narrow line linearly polarized Raman fiber laser to 589 nm". *Opt. Express*, vol.13, no.18:p.6772, 2005, doi:10.1364/OPEX.13.006772.

[75] Y. Feng, L. R. Taylor, and D. B. Calia. "150W highly-efficient Raman fiber laser". *Opt. Express*, vol.17, no.26:p.23678, Dec.2009, doi:10.1364/OE.17.023678.

[76] S. K. Turitsyn, S. A. Babin, D. V. Churkin, I. D. Vatnik, M. Nikulin, and E. V. Podivilov. "Random distributed feedback fibre lasers". *Phys. Rep.*, vol.542, no.2:pp.133–193, Sep.2014, doi:10.1016/j.physrep.2014.02.011.

[77] M. Fernandez-Vallejo, S. Rota-Rodrigo, and M. Lopez-Amo. "Comparative study of ring and random cavities for fiber lasers". *Appl. Opt.*, vol.53, no.16:p.3501, Jun.2014, doi:10.1364/AO.53.003501.

[78] E. B. Mejía and L. de la Cruz-May. "Spectral changes produced by an adjustable intra-cavity Fabry-Perot interferometer inside an ytterbium-doped fiber laser". *Laser Phys.*, vol.25, no.9:p.095101, Sep.2015, doi:10.1088/1054-660X/25/9/095101.

[79] L. Cruz-May and E. B. Mejía. "Raman fiber laser improvement by using Yb^{3+}-doped fiber". *Laser Phys.*, vol.19, no.5:pp.1017–1020, May.2009, doi:10.1134/S1054660X09050235.

[80] E. B. Mejía, L. De la Cruz-May, and D. V. Talavera. "Shortening of a raman fiber laser by inserting ytterbium doped fiber". *IOSR J. Eng.*, vol.3, no.12:pp.38–43, Dec.2013, doi:10.9790/3021-031213843.

[81] J. W. Nicholson, T. Taunay, E. Monberg, F. DiMarcello, Y. Li, and J. Ng. "All-in-one 1236-nm Yb/Raman fiber laser". *Fiber Lasers IX Technol.Syst.Appl.(Proc.SPIE)*, vol.8237, no.823733:pp.38–43, Feb.2012, doi:10.1117/12.908758.

[82] J. Z. Wang, Z. Q. Luo, Z. P. Cai, M. Zhou, C. C. Ye, and H. Y. Xu. "Theoretical and experimental optimization of O-band multiwavelength mixed-cascaded phosphosilicate raman fiber lasers". *IEEE Photonics J.*, vol.3, no.4:pp.633–643, Aug.2011, doi:10.1109/JPHOT.2011.2159263.

[83] S.T. Davey, D.L. Williams, B.J. Ainslie, W.J.M. Rothwell, and B. Wakefield. "Optical gain spectrum of $GeO_2 - SiO_2$ Raman fibre amplifiers". *IEE Proceedings J (Optoelectronics)*, vol.136, Issue 6:pp.301–306, Dec.1989, doi:10.1049/ip-j.1989.0047.

[84] F. L. Galeener, J. C. Mikkelsen Jr., R. H. Geils, and W. J. Mosby. "The relative Raman cross sections of vitreous SiO_2, GeO_2, B_2O_3 and P_2O_5". *Applied Physics Letters*, vol.32, Issue 1:pp.215–219, 1978, doi:10.1063/1.89823.

[85] M. Juárez-Hernández, E. B. Mejía, L. de la Cruz-May, and O. Benavides. "Stokes-to-Stokes and anti-Stokes-to-Stokes energy transfer in a Raman fibre laser under different cavity configurations". *Laser Phys.*, vol.26, no.11:pp.115105, Nov.2016, doi:10.1088/1054-660X/26/11/115105.

[86] R. H. Stolen, C. Lee, and R. K. Jain. "Development of the stimulated Raman spectrum in single-mode silica fibers". *J. Opt. Soc. Am. B*, vol.1, no.4:pp.652, Aug.1984, doi:10.1364/JOSAB.1.000652.

[87] N. Park, J. W. Dawson, K. J. Vahala, and C. Miller. "All fiber, low threshold, widely tunable single-frequency, erbium-doped fiber ring laser with a tandem fiber Fabry-Perot filter". *Appl. Phys. Lett.*, vol.59, no.19:pp.2369–2371, Nov.1991, doi:10.1063/1.106018.

[88] Y. J. Rao. "In-line fiber-optic etalon formed by hollow-core photonic crystal fiber". *Asia Optical Fiber Communication and Optoelectronics Conference*, pages pp.124–126, Oct.2007, doi:10.1109/AOE.2007.4410725.

[89] E. B. Mejía, L. de la Cruz-May, and J. F. Vásquez-Jiménez. "Temperature control of power distribution on the Stokes components of a Raman fiber laser". *Laser Phys.*, vol.24, no.5:pp.055103, May 2014, doi:10.1088/1054-660X/24/5/055103.